國立臺灣大學理學院物理學研究所

碩士論文

Department of Physics

College of Science

National Taiwan University

Master Thesis

應用雙光子顯微術觀察油酸對皮膚滲透動態傳輸之影響

Two-Photon Visualization of Transport Dynamics

in Oleic Acid-Induced Transdermal Delivery

許訓嘉

Hsin-Chia Hsu

指導教授: 董成淵 博士

Advisor : Chen-Yuan Dong, Ph.D.

中華民國 99 年二月

February, 2010

國立臺灣大學（碩）博士學位論文
口試委員會審定書

論文中文題目

應用雙光子顯微術觀察油酸對皮膚滲透動態傳輸之影響

論文英文題目

Two-Photon Visualization of Transport Dynamics in Oleic Acid-Induced Transdermal Delivery

本論文係許訓嘉君（學號 r96222020）在國立臺灣大學物理學系、所完成之碩士學位論文，於民國 98 年 10 月 15 日承下列考試委員審查通過及口試及格，特此證明

口試委員：

（簽名）

（指導教授）

致謝

　　時光匆匆，2.5 年的碩士班生涯隨著論文的完成而接近尾聲了。在這段旅程之中首先要感謝的是我的指導老師　董成淵教授。　董老師在指導學生的時候總是透過引導的方式讓我們能夠一步一步的學習去整理出正確而且完整的邏輯，並且常常能夠從新的視角來幫助我們找到研究的切入點和看見研究的價值，也經常和我們分享在研究發表的過程當中的一些經驗和抹角，讓我們在受到科學研究訓練的同時也更加了解學術研究的環境。雖然有點遺憾並沒有能完成老師當初交給我的腦神經的 project，但是我相信未來隨著實驗室儀器的升級，一定有機會能夠進軍腦神經領域的。另外也要感謝師母　Jen 在我剛進實驗室還不知道要做什麼的時候帶我一起唸生物學，並且教我認識和操作實驗室的儀器設備。而在辦公室吃著點心和您談論研究心得和房地產仲介的內幕的那段時光也讓我印象深刻，預祝您在未來能實現您的夢想成為一位生命科學的研究工作者。

　　除了需要明師的指點，學習的環境同樣不可或缺，正因為在各方面受到了許多人的協助我的研究才得以完成。首先要感謝 專業且充滿樂活精神的　Wesly:在口試之後論文的修改對沒有發表經驗的我來說是一個浩瀚的工程，這時候感謝 Wesly 不辭勞苦的幫忙，從文法、遣詞用字、內容的拿捏、排版到未來進一步實驗的建議都逐一的和我討論修改。而　Wesly 從容自在而愜意的生活方式也讓平時比較拘束的我對生活有了新的體會。再來要感謝的是認真且熱心助人的駱文學姊:在我需要新的 project 的時候給了我這個這個方向，提供數據分析的建議並且幫我寫了關鍵的 IDL 分析程式。實力堅強且思慮周詳的　Vova:在我嘗試 collagen photodenature project 的期間給了我很多至今受用的聰明 ideas，還有提醒我看更深入看 paper 的方法。見多識廣且風趣的峰杰學長:實驗室光學系統的工作原理在經過你的講解之後似乎都變得簡單了，很多實驗上的考量也都經過你的解說才了解。率真且開朗的小美:在面對複雜的數據圖表而不知如何解釋的時候多虧妳幫我找出一條思路才有後續的分析工作。內斂且忙碌的俊欽:感謝你教我如何照顧裸

I

鼠，還有 sample 的保存方法。虔誠且在學術界交遊廣闊的秉榮:感謝你總是認真的幫我解決實驗過程中的狀況並且給我很多鼓勵。醫工所風度翩翩的德軒學長:感謝你教我關鍵的固定 sample 的技術還有對研究方向的建議。

凝態中心林老師麾下的博士後小忱:從我認識你開始就不斷的受到你的指導無論是在研究上或是人生觀上，祝你未來能早日找到教職。

薄荷綠地的 Amy 黃逸美老師，讓我能夠在每次這麼 high 的上課氣氛中 讓自己的心跟視野都更加的擴展，祝妳的生命愈來愈圓滿。

還有期待早日畢業的生活知識家若雅:妳可以心想事成的。尋找博士題目的投手志儒:恭喜你通過必修課的挑戰了，祝你找到有發展性跟前瞻性的好題目。LIVER組的單傳弟子書硯:穩穩的做一定沒問題的，老師的肝就靠你們了。衝勁十足的蔡董:加油，開春前兩炮有機會是你喔。碩一的威翔、宗翰:祝你們修課順利有機會多了解實驗室的 projects 會比較快上手喔。天文所的馬尾兄，感謝你教我這麼實用的生活資訊，讓我現在有塞爆兩顆硬碟將近 600GB 的電影可以看。也祝你順利畢業、入伍。已經畢業的聖舜、聿揚、光育、培修，以及學長梓凌、政寬、鈺林、宗憲、嘉旭，助理康薇，謝謝你們的陪伴與分享讓我的生活更豐富更生動。

最後要感謝我的父母給我這麼多的關懷和支持讓我得以專注在我想做的事情上，並且維持一個舒適溫暖的家讓我得以在其中安心的修養。

得之於人者太多，出之於己者太少，除了對所有人表達誠摯的感謝之外，也期望我未來能有更多成長，對這個社會有更多的貢獻。

摘要

我們使用雙光子螢光顯微術來觀察裸鼠皮膚的角質層在 240 分鐘之內經由油酸增強的跨皮膚滲透過程。硫化若丹明 B (SRB)被使用作為模擬極性分子的跨皮膚滲透。一種對極性敏感的染劑，若丹，被使用來監控角質層內極性環境的變化。極化的程度可以透過總體極化量(GP)參數值(-1<= GP <=1)來決定。其中高 GP 值對應非極性環境而低GP則對應極性環境。在滲透過程中所使用的溶劑為磷酸鹽緩衝溶液與乙醇以 1:2 體積所形成的混合液，此為控制組溶液，實驗組溶液則加入額外 3%體積的油酸。

我們的結果顯示出在沒有油酸加入的情況下，極性分子較容易經由角質細胞間質區域滲透而非極性分子比較容易穿過角質細胞內部滲透。油酸的加入不只增加 SRB 分子滲透速率，也增加達到穩定態滲透的速率。再者，油酸的加入導致在皮膚表面以下 10 微米的距離內的 GP 值的增加的現象說明了加入油酸不只改善極性分子(如 SRB 或水分子)的滲透連帶的溶液中其他有較高 GP 值的成分如乙醇，DMSO 的滲透亦被增強。油酸的加入同時也使得角質內部角質細胞間質與角質細胞內部的 SRB 強度與 GP 值的分布比較均勻，以及角質內部角質細胞間質與角質細胞內部之間的滲透增強。

關鍵字: 雙光子螢光顯微術，角質層，硫化若丹明B， 若丹極化率，油酸，乙醇，角質細胞間磷脂質，相分離。

Abstract

We used two-photon fluorescence microscopy to observe 240 minutes of the oleic acid-enhanced transdermal permeation process in the stratum corneum (SC) of nude mouse skin. Sulforhodamine B (SRB) was used to simulate the transdermal delivery of polar molecules. A polarity-sensitive probe, Laurdan, was used to monitor the environmental polarity in SC. The degree of polarity is determined by the general polarization (GP) parameter ($-1 \leq$ GP ≤ 1) with a high GP value for non-polar environment and a low GP value for polar environment. The solvent used for the permeating process was a mixture of phosphate buffered saline and ethanol in a 1:2 ratio by volume for the control group. For the experimental group, an additional 3% by volume of oleic acid was added.

Our results show that without the addition of oleic acid, polar molecules preferentially permeate through the intercellular regions while non-polar molecules preferentially permeate through the intracellular regions. The addition of oleic acid greatly increased not only the permeation rate of SRB, but also the rate that the steady state permeation rate is reached. Furthermore, the addition of oleic acid leads to an increase in the GP value within 10 μm of skin surface suggesting that oleic acid improves the permeation of not only polar molecules (SRB, water) but also other higher GP values components in the solution such as ethanol and DMSO (dimethyl sulfoxide).

The addition of oleic acid results in a more homogeneous distribution of SRB intensity and GP values in both intercellular and non-intercellular region of SC, and an enhancement of the permeation between intercellular region and intracellular region.

Keywords: two photon fluorescence microscopy, stratum corneum (SC), Laurdan GP, sulforhodamine B (SRB), oleic acid, ethanol, intercellular phospholipids, phase separation.

Table of Content

Figure Catalog

VIII

Chapter 1 Introduction

Transdermal drug delivery has been in active development for the past three decades for replacing the traditional oral delivery and hypodermic injection. This development is motivated by the fact that oral delivery often has a large fraction to be metabolized by the first-pass effect and hypodermic injection has the disadvantages of causing pain and needle usage.

The main idea of transdermal drug delivery is to transport the drug molecules through the epidermis to the capillary rich dermis for drug absorption. The main challenge for transdermal drug delivery is to penetrate the outermost layer of skin, stratum corneum (SC), which is composed of corneocytes which contain cross-linked keratin filaments and lipid-rich intercellular space, with a thickness about $10 \sim 30$ μm for humans. Techniques of transdermal drug delivery include changing the structure of skin to lower the resistance for permeation, and imparting extra driving forces to allow the drug molecules to penetrate the skin. For example, chemical enhancers such as DMSO (dimethyl sulfoxide) can extract the intercellular lipid multilayers to reduce the barrier function of multilayers to facilitate drug penetration, while in iontophoresis, an electrical driving force propels charged particles through the skin. Similarly, in electrophoresis, weakly charged or uncharged particles are permeated by electro-osmotic force of water.

Other techniques such as cavitational ultrasound, thermal ablation, microneedles, and electroporation help permeation of larger molecular weight particles and target their effects on the SC. Since the first approval in 1979, there are currently at least 19 transdermal delivery systems approved by the Food and Drug Administration (FDA) in the United States. The approval rate over the last 5 years is approximately one new system for every 7.5 months, suggesting that there is a large future market for transdermal drug delivery technologies[1].

Among the various transdermal systems, there is a long history for using chemical enhancer. The main action of chemical enhancers is to disorder the structure of the stratum corneum such that drugs can permeate into skin. In recent years, there has been active research using biochemical enhancer such as specific peptide and multiple combinations of chemical enhancers to improve the delivery enhancement while reducing skin irritation[2-3].

Oleic acid, a well known chemical enhancer, is a cis-unsaturated fatty acid with a single double bond. The kink structure in oleic acid limits the ability of phospholipid to pack closely, resulting in a lower membrane melting temperature and an increase in skin permeability. Previous research found that cis-unsaturated fatty acids partition into fluid-like phase of membrane, while trans-unsaturated and saturated preferentially partition into solid-like domain[4].

Conventionally, real-time transdermal delivery has been observed through particles flux measurement by high performance liquid chromatography (HPLC) which can be used for quantitative analysis of molecular component of liquid mixture. Such flux measurement, however, does not provide any structural or morphological information. In contrast, two-photon fluorescence microscopy allows real-time imaging of the permeation process, providing information about time-dependent structural and morphological change in the SC. The information can help us understand the mechanism of transdermal permeation, build a dynamical model for transdermal permeation, and gain insights into the appropriate time to use chemical enhancer for optimal enhancement and skin safety. In this thesis, time-lapsed, two-photon microscopy was used to image the dynamical transport of oleic acid induced transdermal delivery. Sulforhodamine B (SRB) in solution of ethanol and PBS in (2:1) ratio with and without 3% (v/v) oleic acid added were placed in contact with the outer surface of nude mouse skin. The use of polar SRB molecules simulates the permeation of polar drugs. By presoaking the skin in Laurdan, we used its fluorescence emission's environmental dependence to monitor the polarity of the skin SC. In addition to revealing the mechanism of the transdermal delivery of SRB, our results also demonstrated two-photon microscopy is an excellent technique to monitor the dynamical transport of transdermal permeation.

Chapter 2   Basic Principles

2.1   Skin Structure

The mammalian skin consists of three parts: epidermis, dermis, and subcutaneous fat. Based on cell morphology, the structure of epidermis can be divided, from the outmost surface, into stratum corneum, stratum granulosum, stratum spinosum, and stratum basale. The interface between the epidermis and the dermis is a wavy basement membrane consisting of type IV collagen which is linked to the extracellular matrix in the dermis by the anchoring fibrils of type VII collagen. The area where the epidermis extends into dermis is called the epidermis reteridge, and the rise of the dermis into epidermis is called the dermal papilla. In the dermis, there are rich neural receptors for the tactile sense, collagen fibers for structural support, and elastic fibers for elasticity of skin. In addition, micro capillary circulation net, abundant sebaceous glands, sweat ducts, cells and hair follicles are also found in the dermis. The subcutaneous fat prevents the escape of body heat, relaxes the irritation from outer world, and stores excess energy. In the epithelium, the thickness of stratum corneum is about 30 μm, the viable dermis (stratum granulosum, spinosum, basale) is about 100 μm, and the thickness of the dermis can as thick as several millimeters. The thickness of subcutaneous fat has a larger region from

few millimeters to several tens millimeters, depends on different parts of body and the

extent of fat content
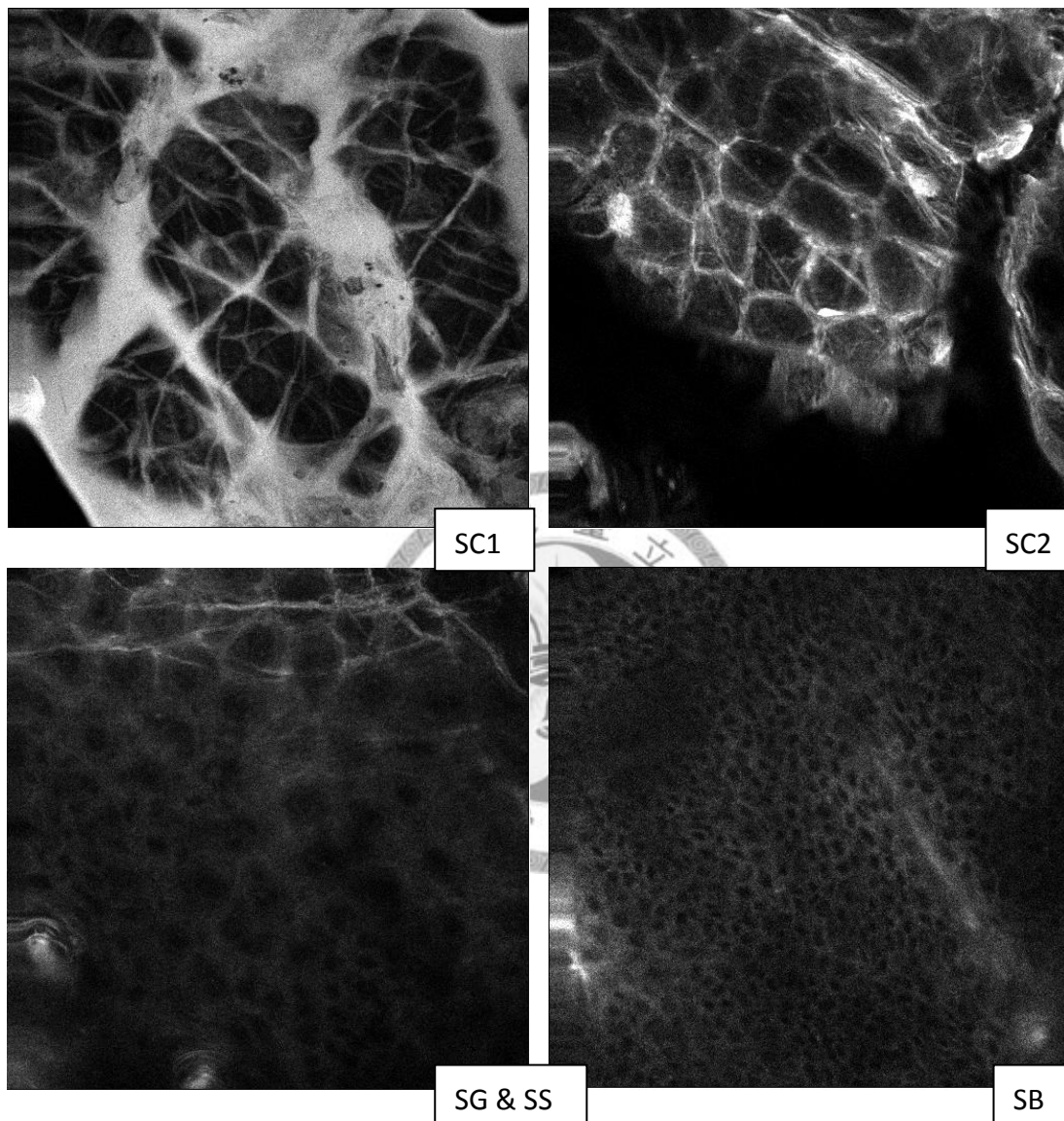
Figure 2-1. Layers of epidermis: stratum corneum (SC), stratum granulosum (SG), stratum spinosum (SS), stratum basale (SB).

There are three main pathways for transdermal drug delivery: intercellular,

transcellular, and hair follicle pathway. In the intercellular pathway, drugs pass through

the hydrophobic intercellular lipid multilayers, while in the transcellular pathway, drugs

partly pass through the hydrophilic keratin-rich corneocytes. Finally, the hair follicle

pathway, which holds only 0.1% surface area of skin, can directly transport particles into

the dermis.
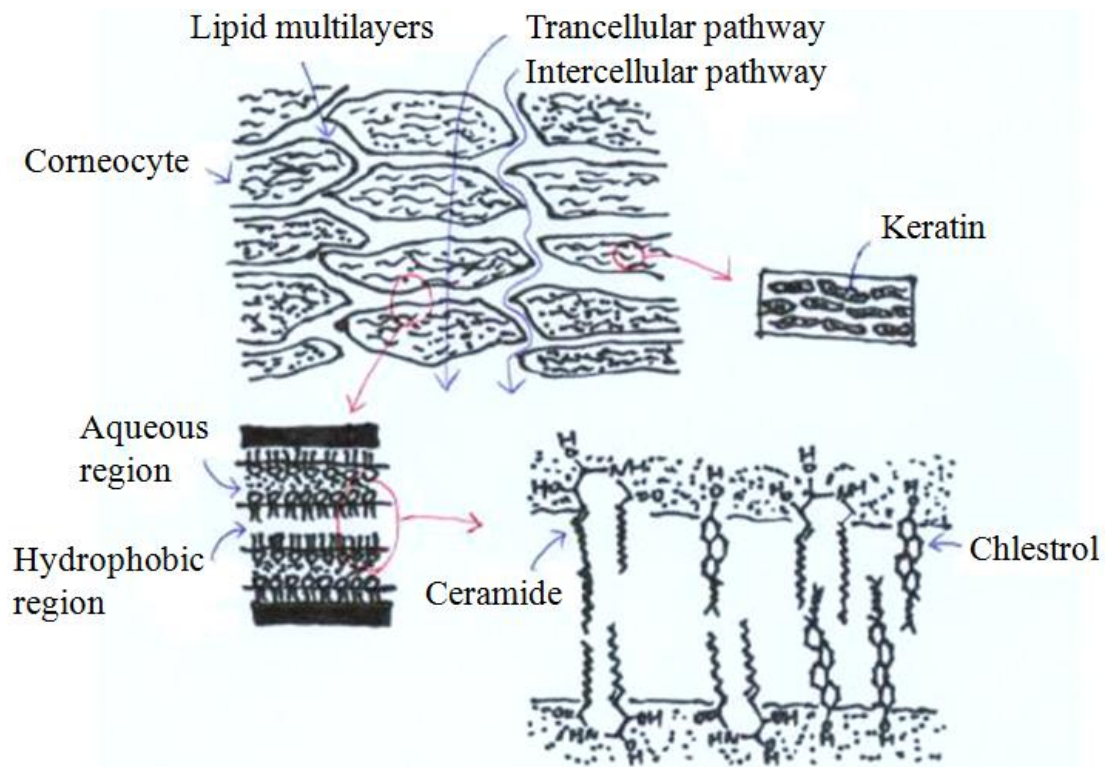
Figure 2-2. Structure of stratum corneum (SC) and the transdermal pathways.

2.2   Fluorescence Properties of Laurdan
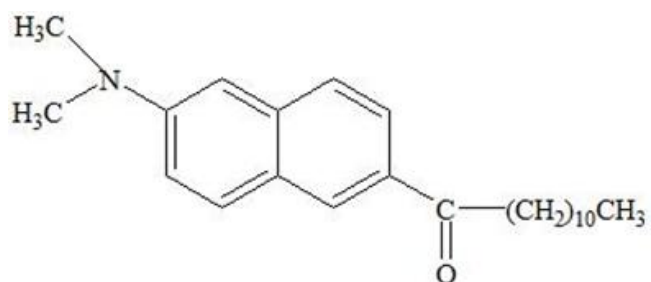
Figure 2-3. Structural formula of Laurdan.

Laurdan (2-Dimethylamino-6-1auroylnaphthalene, MW: 353.55) as a hydrophobic

dye is a derivative of Prodan which was introduced by Weber and Farris in 1979.

Although both prodan and Laurdan can be used to detect membrane fluidity, prodan is

localized at the surface of membrane bilayers, while Laurdan aligns itself parallel to the

hydrophobic tails of the phospholipids in the membrane as shown in Fig. 2-4.
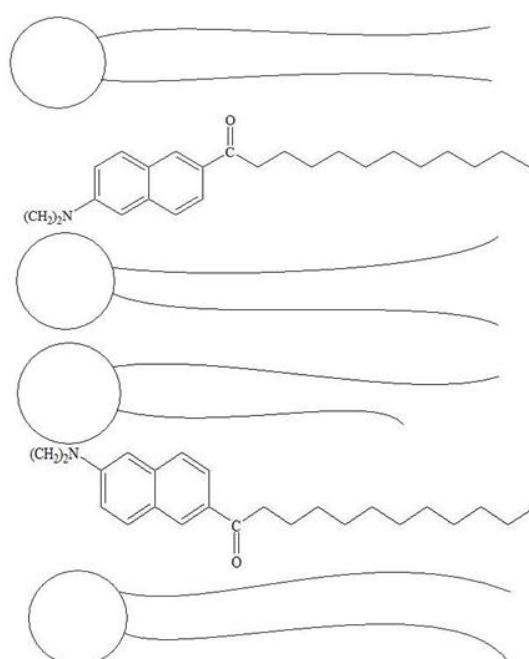
Figure 2-4. Location of Laurdan in phospholipid membrane.

The emission spectrum of Laurdan is solvent-polarity dependent. In non-polar

environment such as DMSO, Laurdan has its peak emission wavelength at about 440nm

(a significant two-photon cross section of excitation at 780~800 nm). In a more polar

environment, Laurdan shows a greater charge separation that results in an increase in its

dipole moment. This leads to an internal charge transfer process that cause a red shift in

the Laurdan emission peak to 490 nm.
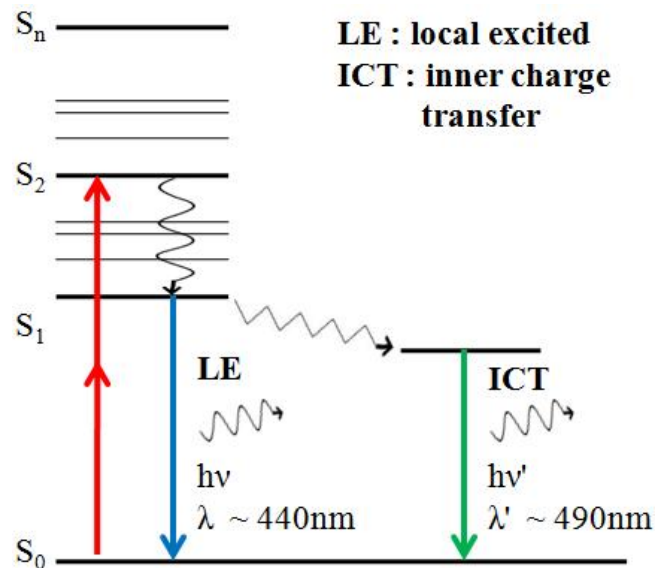
Figure 2-5. Locally excited (LE) state and inner charge transfer (ICT) states of Laurdan.

The environmental dependence of Laurdan emission property makes it an effective probe of membrane packing order. When the packing of the phospholipids in the membrane become increasingly disordered, the membrane will become more permeable to water, exposing the Laurdan on the membrane to a more polar environment, and causing its emission peak wavelength to shift from 440 nm to 490 nm. To quantify the environment polarity with Laurdan fluorescence, it is convenient to define a generalized polarization (GP value) parameter:

$$GP = \frac{I_{440nm} - I_{490nm}}{I_{440nm} + I_{490nm}}$$

For GP value closer to 1, the 490 nm emission intensity is weak, which implies a more ordered membrane packing, and less water permeability. On the other hand, a GP

value closer to -1 indicates a more disordered membrane packing, and greater water

permeability.

2.3   Two-Photon Excitation[5]

2.3.1   Single-Photon Excitation

In the quantum mechanics, a single particle evolving with time can be described by a

time-involved wave vector $\mid \varphi(t) >$ in the physical Hilbert space, defined as the space

of vectors that can be either normalized to unity or to the Dirac delta function. The

projection of a wave vector onto the spatial basis $\mid x >$ is known as a wave function

$\psi(x, t)$.

Time evolution of a single particle in a potential $V(\vec{x}, t)$ follows the Schrodinger

equation:

$$i\hbar \frac{\partial \psi(\vec{x}, t)}{\partial t} = H\psi(\vec{x}. t) \tag{1}$$

where

$$H = T + V = -\frac{\hbar^2}{2m} \frac{\partial^2}{\partial \vec{x}^2} + V(\vec{x}, t)$$

is the Hamiltonian of system. For time-independent potential, separation of variables

allows the wave functions associated with the energy eigenstates to be represented by :

$$\psi_n(\vec{x}, t) = u_n(\vec{x})e^{-i\omega_n t} \text{ , where } \omega_n = \frac{E_n}{\hbar} \tag{2}$$

$$Hu_n(\vec{x}) = E_n u_n(\vec{x})$$

$$\int_{-\infty}^{\infty} u_m^* u_n d^3 r = \delta_{nm} \tag{3}$$

The wave function is a linear combination of energy eigenfunctions :

$$\psi(\vec{x}, t) = \sum_n c_n \psi_n(\vec{x}, t) = \sum_n c_n \, u_n(\vec{x}) e^{-i\omega_n t} \tag{4}$$

For a time-dependent perturbation of the potential

$$V = V_0 + V(t) \quad , \; |V(t)/V_0| \ll 1$$

$$H = T + V = H_0 + V(t) \tag{5}$$

Using Eq. (3), we can write:

$$\psi(\vec{x}, t) = \sum_n c_n(t) \psi_n(\vec{x}, t) = \sum_n c_n(t) \, u_n(\vec{x}) e^{-i\omega_n t} \tag{6}$$

Substitution of (6) into (1) gives

$$i\hbar \sum_n \frac{\partial c_n(t)}{\partial t} u_n(\vec{x}) e^{-i\omega_n t} + i\hbar \sum_n -i\omega_n c_n(t) u_n(\vec{x}) e^{-i\omega_n t}$$

$$= \sum_n E_n u_n(\vec{x}) c_n(t) \, e^{-i\omega_n t} + \sum_n V(t) u_n(\vec{x}) c_n(t) \, e^{-i\omega_n t} \tag{7}$$

Using the orthonormality condition of Eq. (3), we multiply both sides of (7) by

$u_m^*(\vec{x})$ and then taking all space integration to obtain

$$i\hbar \frac{\partial c_m(t)}{\partial t} = \sum_n c_n(t) \left[\int u_m^*(\vec{x}) V(t) u_n(\vec{x}) d^3 r \right] e^{-i\omega_{nm} t} = \sum_n c_n(t) V_{mn} \, e^{-i\omega_{nm} t} \tag{8}$$

with $\omega_{nm} = \omega_n - \omega_m$.

Since equation (8) cannot in general be solved exactly, an approximated solution

can be obtained by perturbation method. This is achieved by substituting a zero-order

value for $c_n(t)$ into (8) and solving for the first order solution. Substituting the first

order solution into Eq. (8) to find the second order solution. This process is iterated to

obtain higher order solutions. In other word, we introduce a small parameter λ corresponding to the order, so $c_n(t)$ can be expanded as

$$c_n(t) = c_n^0(t) + \lambda c_n^{(1)}(t) + \lambda^2 c_n^{(2)}(t) + \ldots \tag{9}$$

The time-dependent perturbation $V(t)$ can be seen as the first order perturbation term such that $V_{mn} \to \lambda V_{mn}$. Substituting $\lambda V_{mn}(t)$ and Eq. (9) into Eq. (8) and collecting the terms with the same power of λ, we obtain the set of equations :

$$i\hbar \frac{\partial c_m^{(N)}(t)}{\partial t} = \sum_n c_n^{(N-1)}(t) \, V_{mn} e^{-i\omega_{nm}t} \quad , \quad N = 1,2,3,\ldots \tag{10}$$

Our goal is to describe a special case of time-dependent absorption that electrons are stimulated by exterior electromagnetic radiation. For simplicity, only single photon excitation is considered.
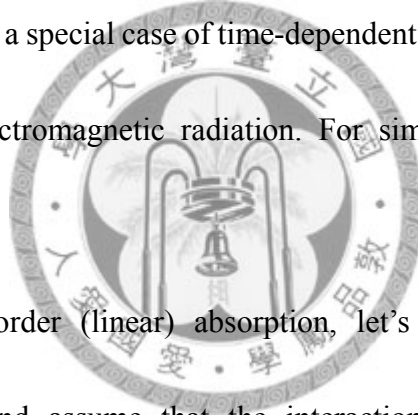
To derive the first order (linear) absorption, let's set $N = 1$ for first order interaction in the field and assume that the interaction potential (time-dependent perturbation) can be represented as :

$$V(t) = -\vec{\mu} \cdot \left(\vec{E}e^{-i\omega t} + \vec{E}^* e^{i\omega t}\right), \; V_{mn} = -\mu_{mn}\left(Ee^{-i\omega t} + E^* e^{i\omega t}\right), \vec{\mu} = -e\vec{r} \tag{11}$$

In the absence of perturbation, the zeroth order amplitudes are:

$$c_n^{(0)}(t) = \delta_{gn} \tag{12}$$

Substituting of (12) into (10), one obtains

$$i\hbar \frac{\partial c_m^{(1)}(t)}{\partial t} = -\mu_{mg}\left[Ee^{i(\omega_{mg}-\omega)t} + E^* e^{-i(\omega_{mg}+\omega)t}\right] \tag{13}$$

Further integration gives

$$c_m^{(1)}(t) = -\frac{\mu_{mg}}{i\hbar} \int_0^t dt' \left[E e^{i(\omega_{mg}-\omega)t} + E^* e^{-i(\omega_{mg}+\omega)t} \right]$$

$$= \frac{\mu_{mg}}{\hbar} \left\{ \frac{E}{(\omega_{mg}-\omega)} \left[e^{i(\omega_{mg}-\omega)t} - 1 \right] + \frac{E^*}{(\omega_{mg}+\omega)} \left[e^{-i(\omega_{mg}+\omega)t} - 1 \right] \right\} \quad (14)$$

The first term corresponds to a resonance when $\omega_m = \omega_g + \omega$ and the second term corresponds to a resonance of when $\omega_m = \omega_g - \omega$. The first term corresponds to the one-photon absorption, while the second term corresponds to the process of stimulated emission. Since our interest is in the stimulated absorption, we drop the second term. As a result, the single-photon excitation probability is given by

$$P_m^{(1)}(t) = \left| c_m^{(1)}(t) \right|^2 \rightarrow \left| \frac{\mu_{mg}E}{\hbar} \right|^2 \left| \frac{e^{i(\omega_{mg}-\omega)t}}{(\omega_{mg}-\omega)} - 1 \right|^2 = \left| \frac{\mu_{mg}E}{\hbar} \right|^2 \left[\frac{sin[(\omega_{mg}-\omega)t/2]}{(\omega_{mg}-\omega)t/2} \right]^2 t^2 \quad (15)$$

We know that in order to have a significant excitation probability, the sinc function $f(x) = \frac{\sin x}{x}$ is considered over the interval $\sim [-\pi, \pi]$. Therefore,

$$(\omega_{mg} - \omega)t/2 \leq \pi \rightarrow E_m \leq E_g + \hbar\omega + \frac{2\pi\hbar}{t} = E_g + \hbar\omega(1 + \frac{2\pi}{\omega t}) \quad (16)$$

As time increases, the particle has increasing probability to be in the excited state.

When the system is exposed to the perturbation for a long time, i.e. $t \rightarrow \infty$, integration of (13) for time from $-\infty \rightarrow \infty$ gives

$$c_m^{(1)}(\infty) = -\frac{\mu_{mg}}{i\hbar} \int_{-\infty}^{\infty} dt' \left[E e^{i(\omega_{mg}-\omega)t} \right] = -\frac{2\pi\mu_{mg}E}{i\hbar} \delta(\omega_{mg} - \omega) \quad (17)$$

$$P_m^{(1)}(\infty) = \left| c_m^{(1)}(t) \right|^2 \rightarrow \left| \frac{2\pi\mu_{mg}E}{\hbar} \right|^2 \delta(\omega_{mg} - \omega)\delta(\omega_{mg} - \omega) \quad (18)$$

Introducing the treatment of $\delta\delta$ previously introduced[6]

$$\delta\delta = \lim_{t\to\infty} \delta(\omega_{mg} - \omega) \frac{1}{2\pi} \int_{-\frac{t}{2}}^{\frac{t}{2}} dt' \left[e^{-i(\omega_{mg}-\omega)t'} \Big|_{\omega_{mg}=\omega} \right]$$

12

$$= \delta(\omega_{mg} - \omega) \lim_{t\to\infty} \frac{t}{2\pi} \tag{19}$$

results in

$$P_m^{(1)}(t) = \left|\frac{\mu_{mg}E}{\hbar}\right|^2 2\pi t \delta(\omega_{mg} - \omega) \tag{20}$$

In physical reality, the excited state is not a single state, but a spread in the energy interval, so we can define a density of state ρ_m such that $\rho_m(\omega_{mg})d\omega_{mg}$ is the probability that the particle makes a transition with the excitation frequency between ω_{mg} and $\omega_{mg} + d\omega_{mg}$ such that

$$\int_0^\infty \rho_m(\omega_{mg})d\omega_{mg} = 1 \tag{21}$$

Next, we integrate the contribution of the density of states to obtain the complete transition probability

$$P_m^{(1)}(t) = \left|\frac{\mu_{mg}E}{\hbar}\right|^2 2\pi t \int_0^\infty \rho_m(\omega_{mg})\delta(\omega_{mg} - \omega) \, d\omega_{mg} = \left|\frac{\mu_{mg}E}{\hbar}\right|^2 2\pi t \rho_m(\omega) \tag{22}$$

After division by t, the transition rate of linear absorption becomes

$$R_{mg}^{(1)} = \frac{P_m^{(1)}}{t} = 2\pi \left|\frac{\mu_{mg}E}{\hbar}\right|^2 \rho_m(\omega) \tag{23}$$

which is Fermi's golden rule.

2.3.2 Two-Photon Excitation

To find the transition rate for two-photon excitation, set $N = 2$ in (10) and substitute the first order solution Eqn. (14) into the second order equation. By keeping the term corresponding to absorption, one obtains

$$i\hbar \frac{\partial c_n^{(2)}(t)}{\partial t} = \sum_m c_m^{(1)}(t)\, V_{nm} e^{-i\omega_{mn}t}$$

$$= \sum_m \frac{\mu_{mg}}{\hbar} \frac{E^2}{(\omega_{mg}-\omega)} \left[e^{i(\omega_{mg}-\omega)t} - 1 \right] V_{nm} e^{-i\omega_{mn}t}$$

$$= \sum_m \frac{-\mu_{nm}\mu_{mg}}{\hbar} \frac{E^2}{(\omega_{mg}-\omega)} \left[e^{i(\omega_{ng}-2\omega)t} - e^{-i(\omega_{nm}-\omega)t} \right] \qquad (24)$$

By only keeping the two-photon absorption term and integrating over time, one has

$$c_n^{(2)}(t) = \sum_m \frac{\mu_{nm}\mu_{mg}}{\hbar^2} \frac{E^2}{(\omega_{mg}-\omega)(\omega_{ng}-2\omega)} \left[e^{i(\omega_{ng}-2\omega)t} - 1 \right] \qquad (25)$$

$$P_n^{(2)}(t) = \left| c_n^{(2)}(t) \right|^2 = \left| \sum_m \frac{\mu_{nm}\mu_{mg}}{\hbar^2} \frac{E^2}{(\omega_{mg}-\omega)} \right|^2 \left| \frac{e^{i(\omega_{ng}-2\omega)t}-1}{(\omega_{ng}-2\omega)} \right|^2$$

$$= \left| \sum_m \frac{\mu_{nm}\mu_{mg}}{\hbar^2} \frac{E^2}{(\omega_{mg}-\omega)} \right|^2 \left[\frac{\sin[(\omega_{ng}-2\omega)t/2]}{(\omega_{ng}-2\omega)t/2} \right]^2 t^2 \qquad (26)$$

Again, if the perturbation time approaches infinity, we obtain

$$P_n^{(2)}(t) = \left| \sum_m \frac{\mu_{nm}\mu_{mg}}{\hbar^2} \frac{E^2}{(\omega_{mg}-\omega)} \right|^2 2\pi t \delta(\omega_{ng} - 2\omega) \qquad (27)$$

For continuous energy states,

$$P_n^{(2)}(t) = \left| \sum_m \frac{\mu_{nm}\mu_{mg}}{\hbar^2} \frac{E^2}{(\omega_{mg}-\omega)} \right|^2 2\pi t \rho_n(\omega_{ng} = 2\omega) \qquad (28)$$

And the two-photon transition rate becomes

$$R_{ng}^{(2)} = \frac{P_n^{(2)}}{t} = \left| \sum_m \frac{\mu_{nm}\mu_{mg}}{\hbar^2} \frac{E^2}{(\omega_{mg}-\omega)} \right|^2 2\pi \rho_n(\omega_{ng} = 2\omega). \qquad (29)$$

For three- and four-photon transition rates, we respectively have

14

$$R_{og}^{(3)} = \frac{P_o^{(3)}}{t} = \left| \sum_{mn} \frac{\mu_{on}\mu_{nm}\mu_{mg}}{\hbar^3} \frac{E^3}{(\omega_{ng}-\omega)(\omega_{mg}-\omega)} \right|^2 2\pi\rho_n(\omega_{og} = 3\omega) \quad (30)$$

and

$$R_{pg}^{(4)} = \frac{P_p^{(4)}}{t} = \left| \sum_{omn} \frac{\mu_{po}\mu_{on}\mu_{nm}\mu_{mg}E^4}{\hbar^3(\omega_{og}-\omega)(\omega_{ng}-\omega)(\omega_{mg}-\omega)} \right|^2 2\pi\rho_n(\omega_{pg} = 4\omega) \quad (31)$$

Chapter 3 Materials and Methods

3.1 Sample Preparation

Skin excised from the abdominal region of sacrificed nude mouse was stored at

-20°C, and used within 2 weeks of experimentation. On the day of the experiment, the

skin was first thawed at room temperature for 20 minutes and cut into 1 cm x 1 cm pieces

for processing. Prior to image acquisition, the skin was soaked in 0.033 mM Laurdan in

phosphate buffered saline (PBS) solution (3.3 mM stock in DMSO) for 14 hrs, then rinsed

and cleaned with PBS and tissue paper. The sample was placed flatly on a cover glass,

with its edges sealed by clay, exposing only the outer surface of the skin to solution

permeation. The clay sealed sample was then placed on the center of a glass bottom dish

(MatTek Corporation, Ashland, MA, USA), and placed on the microscope for imaging.

3.2 Solution Preparation

The contents of the permeating solutions for the control and the experimental group

are listed below:

Control group: 0.1 ml of 3.3 mM Laurdan (stock in DMSO), 0.4 ml of 0.1 mM SRB

(stock in PBS : ethanol = 1:1 v/v solution), 3.1 ml PBS, and 6.2 ml

ethanol.

> 0.033 mM Laurdan & 0.004 mM SRB in PBS : ethanol = 1:2 v/v

solution.

Experimental group: Control group solution added with 0.3ml oleic acid (3% v/v).

Laurdan was added in both groups to maintain constant concentration of Laurdan inside and outside of the sample, preventing the reverse permeation of pre-labeled Laurdan into the stratum corneum.

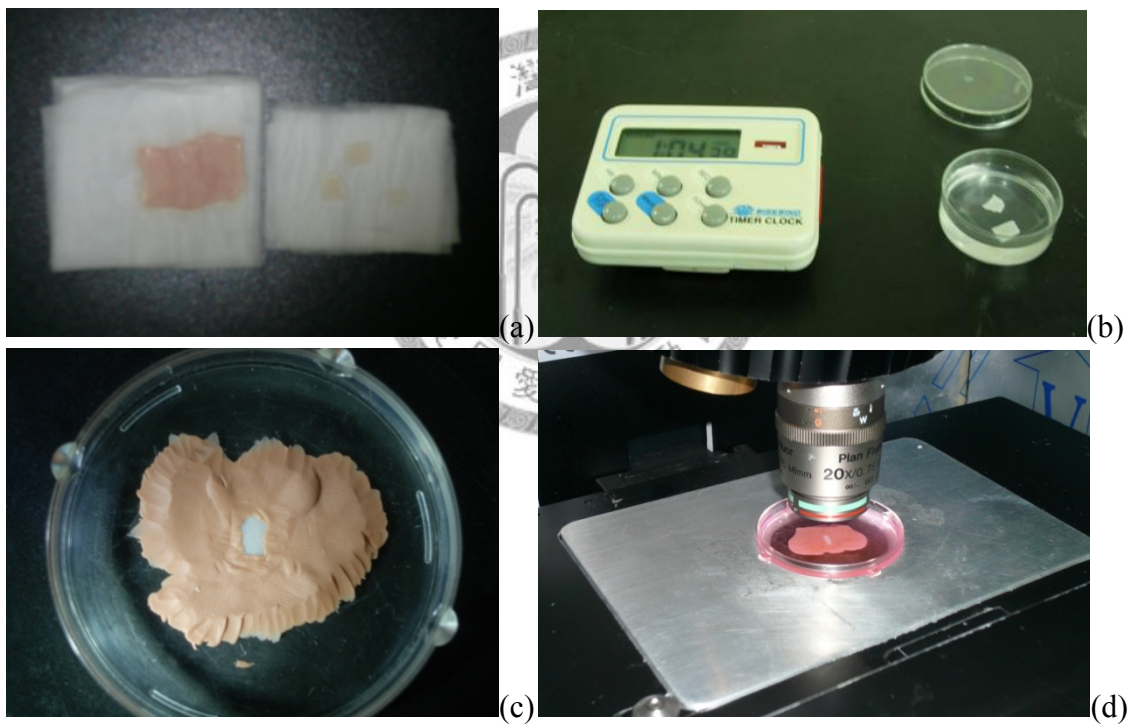Specimen preparation procedures are illustrated in Fig. 3-1.

Figure 3-1. Experimental procedures. (a) Sample unfreezing. (b) Prelabelling Laurdan for 14 hours. (c) Specimen fixation by clay soil. (d) Imaging the permeation of solution.

3.3   Optical Microscopy Setup

Figure 3-2 shows a diagram of the imaging setup.   The excitation source consist of a titanium-sapphire pulse laser (Tsunami, Spectra Physics, Mountain View, California), pumped by a diode laser (Millennia X, Spectra Physics) to produce 780 nm-wavelength near infrared light at a pulse frequency of 80 MHz. The laser beam power is controlled by the combination of half-wave plate and linear polarizer, and a quarter-wave plate is positioned to produces circular polarized laser beam for excitation.

The x-y scanning mirrors system control the movement of the focused laser beam on the sample. A pair of relay lens keeps the beam reflected by the first scanning mirror (x mirror) fixed on the same location of the second scanning mirror (y mirror). The laser beam is expended from 3mm to 40mm to overfill the back aperture of objective, before it is reflected by the main dichroic (700DCSPXRUV-3p, Chroma Technology, Brattleboro, VT).   The short pass main dichroic mirror reflects light with wavelength >700 nm and allows light with wavelength shorter than 700 nm to pass. To image the sample while it is under the permeating solution, a 20x water immersion objective (N.A.=0.75, W.D. = 0.35 mm, Plan Fluo, Nikon, Japan) was used. The fluorescence emission (<700 nm) is collected by the same objective and passes through the main dichotic mirror. Two dichroics (555DCXR, 470DCXR) and three band-pass filters (590/80, 490/40, 440/40) divide the emission fluorescence into three channels (red : 550-630, green : 470-510,

18

blue : 420-460) before signal detection by single photon counting photomultiplier tubes

(R7400P, Hamamatsu, Hamamatsu city, Shizuoka, Japan). The signals from each PMT

output are threshold by a discriminator and counted by the custom controller card on the

computer. The scanning software coordinates the scanning and the signal acquisition to

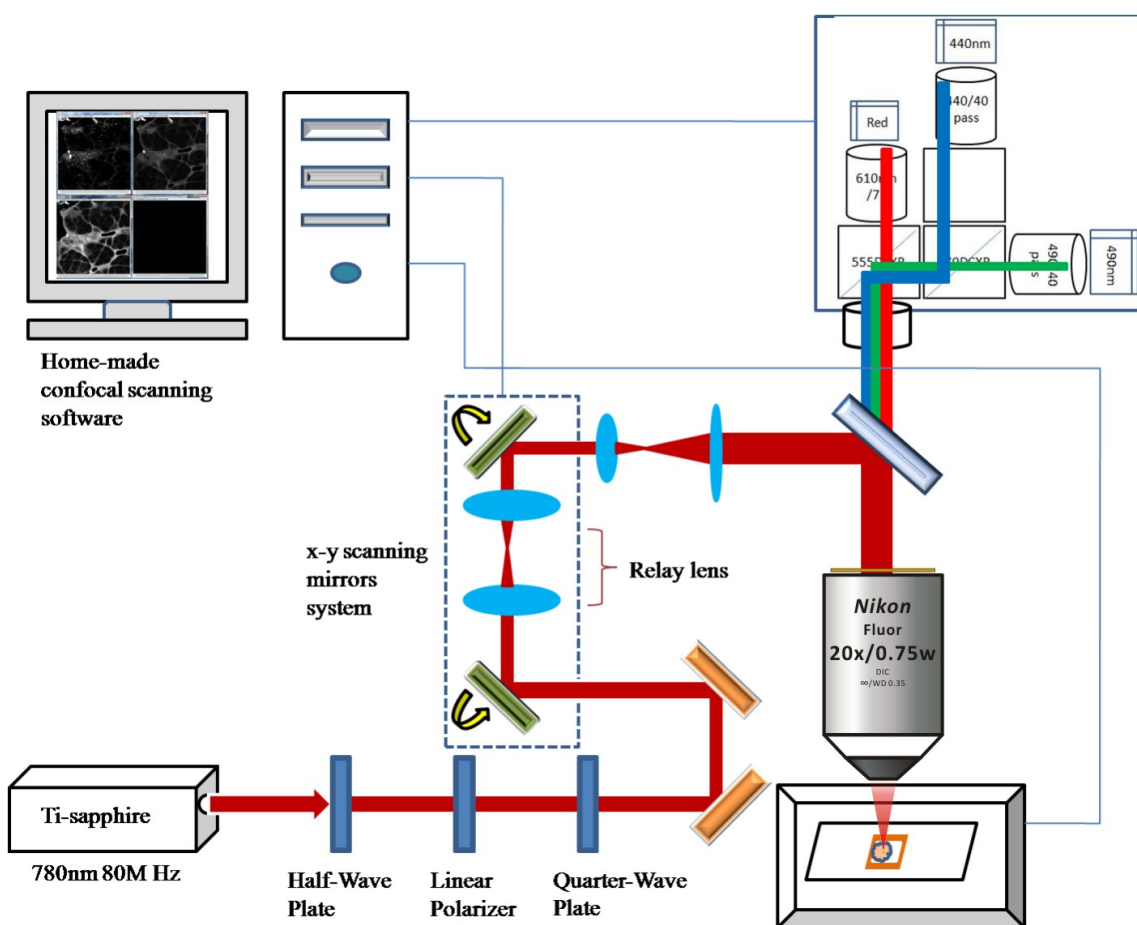display and record the 3-channel images on the monitor.

Figure 3-2. Setup of the Multiphoton Optical Microscope.

Before performing the imaging experiment, the multiphoton microscope was

optimized for field flatness test. Power test were performed to ensure the both emission

fluorescence and PMTs are not in saturation. We started the image acquisition, right

after the addition of the permeating solution. Each 512×512 pixel scanned image covers

a 220×220 μm^2 view of field. 25 images were acquired with depth separation of 3 μm,

covering a total depth of 75 μm.   The z-axis (along depth) scanning was performed once

every 20 minutes for 240 minutes. The scanning rate was 5~6 second/frame.

3.4   Derivation of GP-resolved Images

In Section 2.2, we defined $GP = \frac{I_{440nm} - I_{490nm}}{I_{440nm} + I_{490nm}}$ as a ratio to measure the

environment polarity.   Since the detection efficiency of 440-nm and 490-nm channels

are different, direct substitution of the measured I_{440nm}, I_{490nm} may lead to a significant

deviation in GP value. To adjust for this problem, we rescaled the intensity histogram

distributions of both channels as shown on **Figure 3-3.** For each channel, we divide the

intensity by the average of the highest 1% intensity values in the intensity distribution for

that channel, and calculate the GP value for each non-zero pixels with the rescaled

intensity. For the pixels where either I_{440nm} or I_{490nm} is zero, we assign that pixel an

arbitrary value of -5, to distinguish it from pixels with calculated GP values. The analysis

for the calculating the GP values were performed using a custom IDL program.

Because dimethyl sulfoxide (DMSO) is a non-polar molecules, we expects GP value

of DMSO to be closer to 1. The rescale process changes the GP of DMSO from -0.45 to

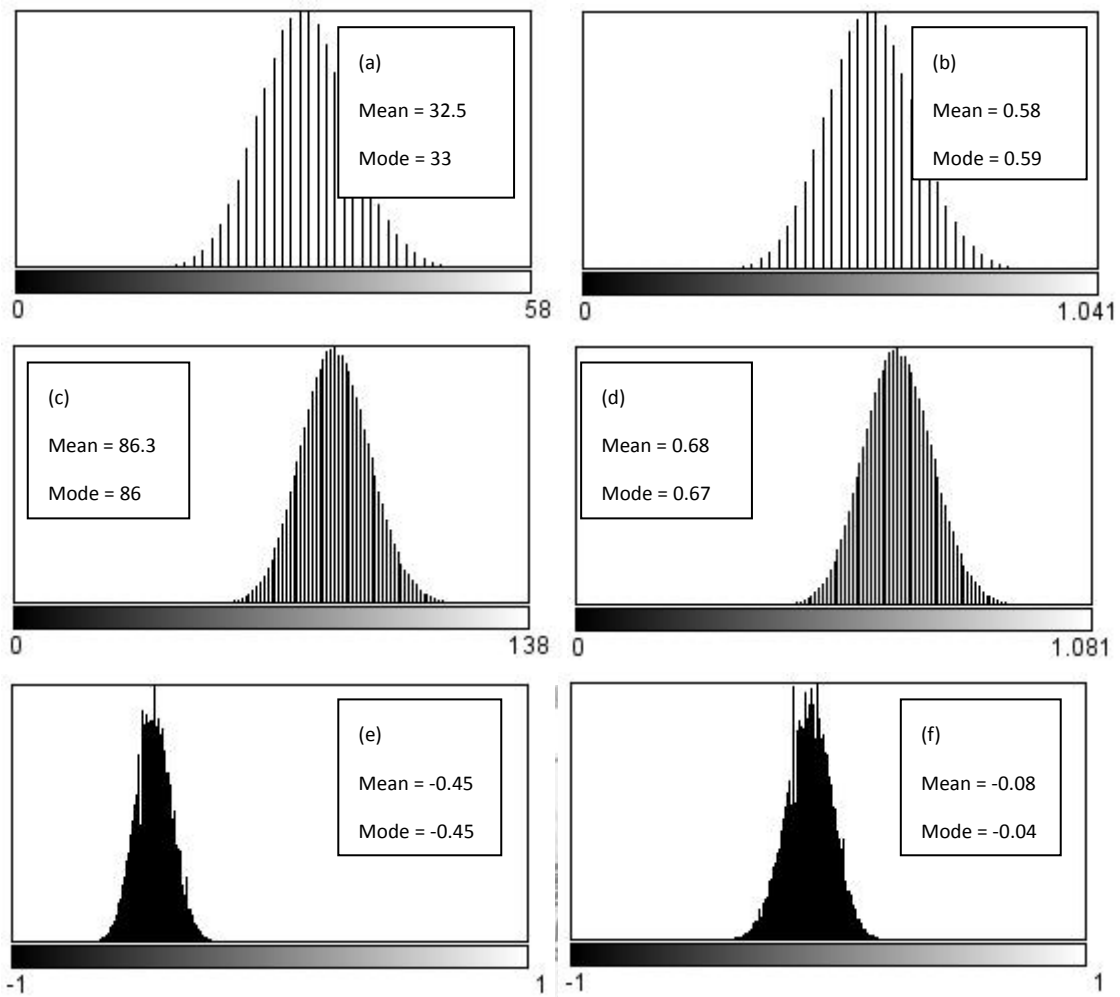0.08, which is more representative of non-polar molecules.

Figure 3-3. GP rescale for Laurdan in DMSO. Intensity distribution of image of (a) Original 440 nm. (b) Rescaled 440 nm. (c) Original 490 nm. (d) Rescaled 490 nm. (e) Direct-calculating GP. (f) Rescaled GP. 20X Water immersion objective, N.A.=0.75 was used, power = 20 mW at the input of the objective. T =20°C.

3.5　Data Analysis

With ImageJ and IDL image processing software, we analyzed the depth-resolved images to obtain SRB intensity curves and the corresponding GP values at each time point. Two type of averaging analysis were performed. The **general average** analysis was done by choosing three random 150 pixels × 150 pixels ($65 \times 65 \ \mu m^2$) squared regions of the

imaged area where the skin surfaces are relatively flat (Figure 3-4 (a)), and averaging the

SRB intensity of the selected region for each of the depth-resolved images to produce a

depth-dependent averaged intensity curve.   This average was done at different times in

order to quantify the time dependence of the permeation depth of SRB molecules and the

variation of GP values. Three samples for each of the control and experimental groups

were used to improve the statistics of the results.

In addition to investigating the universal effect of permeation on SC, we also

investigate the permeation of intercellular phospholipids region in SC, since this

continuous and porous structure region within the stratum corneum is the main pathway

for transdermal permeation[7]. In clinical conditions, most enhancers interact with the

intercellular region[8]. For **specific average** analysis, one intercellular region of the

stratum corneum in each of the square region selected for general average analysis were

chosen. Under this specific average, a 10 pixel wide band surrounding a single corneocyte

was averaged to obtain the time dependence of the permeation of SRB molecules and

variation of GP values in more intercellular regions (Figure 3-4 (a)). 3D volume viewer

plug-in of ImageJ was used to get the vertical cross section view of depth-resolved

images (Figure 3-4 (b)).

Due to the unevenness of the skin surface, some regions in Figure 3-4(a) lie above

the skin surface. These areas have dispersion of large amounts of black points in white

background due to the very low concentration of Laurdan molecules and subsequently

low I_{440nm}, I_{490nm} intensities. The small I_{440nm} and I_{490nm} values led to large swings in the

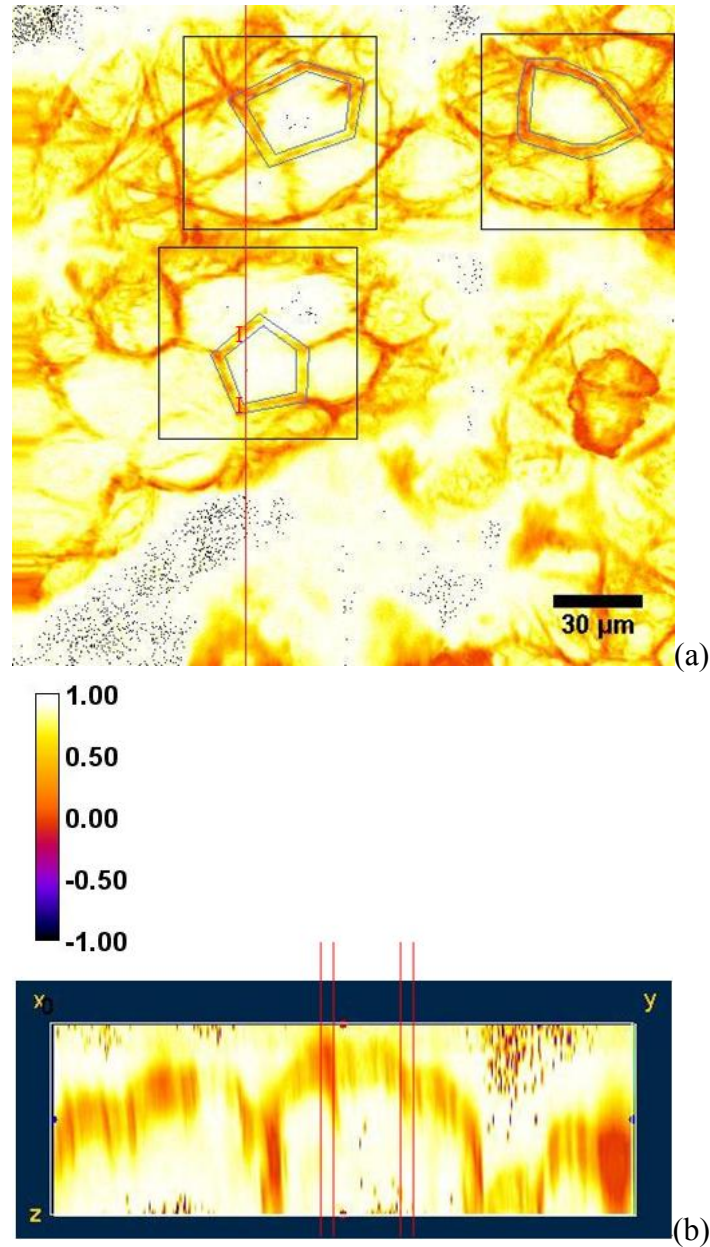calculated GP value, resulting in extreme high (white) or low (black) points.

(a)

(b)

Figure 3-4. GP image analysis. (a) GP imaging with selected regions for general average (quadrate regions) and specific averaging (banded regions) analysis. (b) Cross sectional view through the stack of images for the location indicated by vertical line in (a). Section image construction was performed with ImageJ using the 3D Volume Viewer plug-in.

Chapter 4 Results and Discussions

4.1 GP Measurement for Solutions

GP values for 0.033 mM Laurdan solutions using different solvents are measured to

determine the degree of polarity of each solution. Fig. 4-1 shows the resultant GP values

for each solution combination.   The graph indicates that the addition of oleic acid

increases the polarity of the solution of PBS and ethanol, which implies that the polarity

of oleic acid is larger than the polarity of ethanol. The large polarity of oleic acid is likely

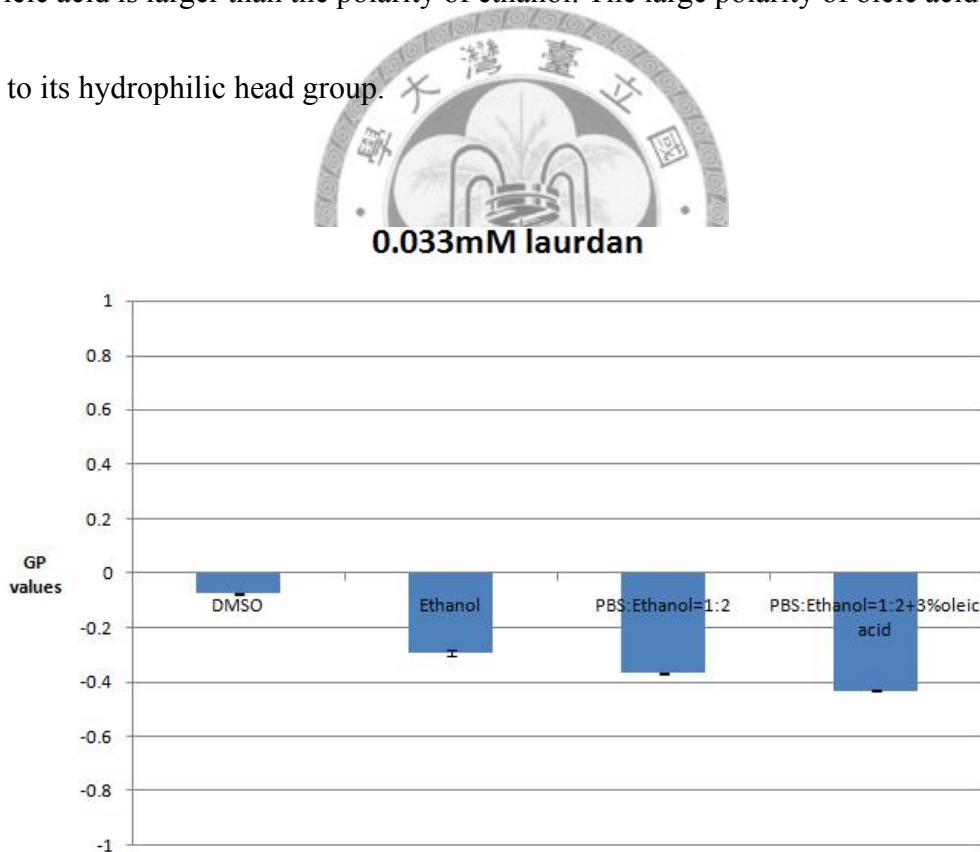due to its hydrophilic head group.

Figure 4-1. GP values for equal concentration of Laurdan solutions in different solvents.

4.2   Variations of SRB Intensity and GP Values

To investigate the effects of oleic acid on the transdermal permeation of SRB molecules, we acquired time-lapsed depth resolved images for skin samples with and without the addition of oleic acid. Figure 4-2(a) shows the SRB intensity images for a skin sample untreated by oleic acid at four different times and depths, with 0 μm denoting the skin surface. The surface of skin is defined as the depth with maximum average SRB intensity, which was determined by using the average over the intercellular region. Typical intercellular region selected for analysis consists of a 10-pixel (~4.3 μm) wide band surrounding a corneocyte (Fig. 3-4(a)). We define 0 μm or the skin surface as the maximal local average of the intercellular SRB intensity.

Control Group – SRB intensity

(a)

Oleic Acid Treated Group – SRB intensity
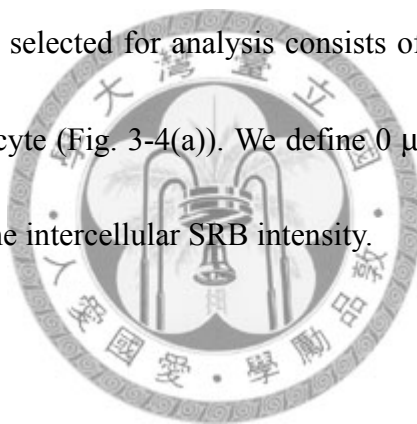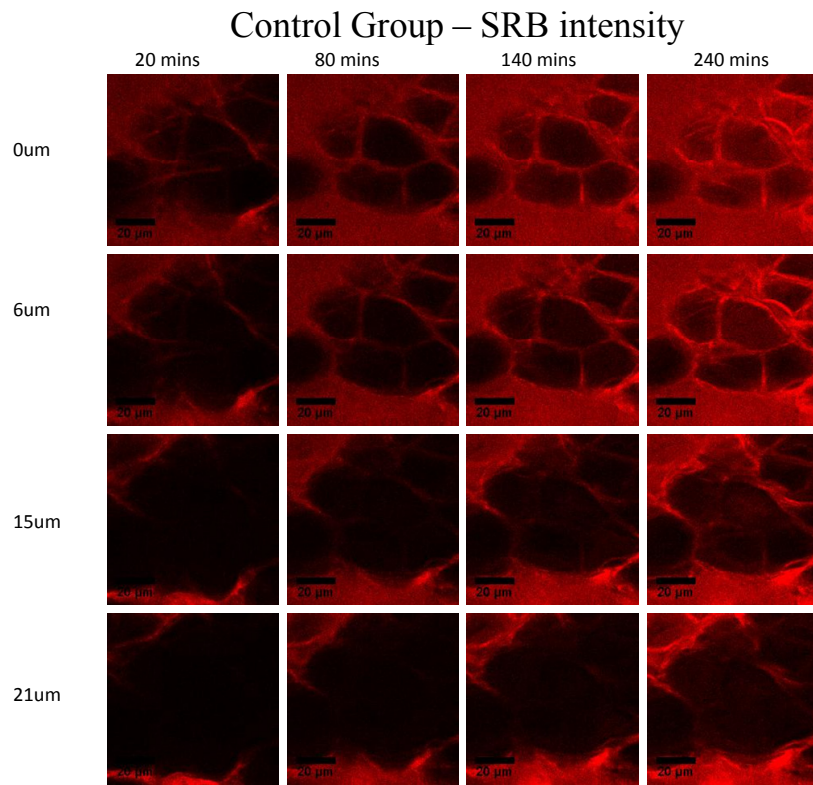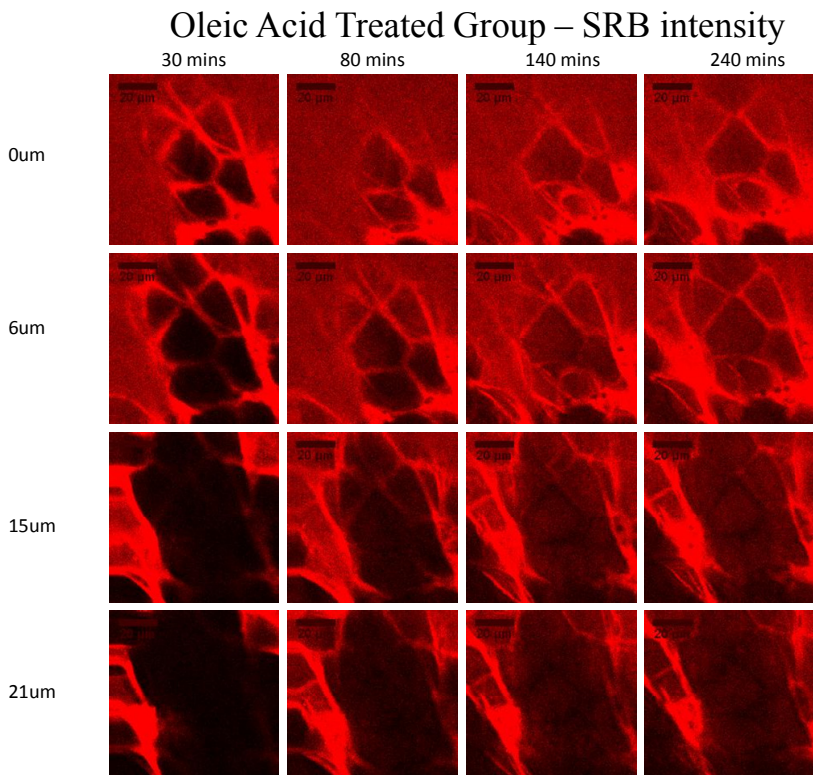
(b)

Figure 4-2. SRB intensity images of one selected region (for general average) at different depth and time point for (a) control and (b) oleic acid-treated groups.

Comparison between the control and the oleic acid-treated images is shown in Figure 4-2. As the images show, the increase of permeating concentration in oleic acid treated skin can be clearly observed. For the 0 μm images of the control group (Figure 4-2(a)), the SRB intensities starts low and becomes progressively brighter in time, with the intensities in the intercellular region greater than the intensities in the intracellular region. For the oleic acid treated skin images, no visible trend of increasing SRB intensity is observed. However, quantitative plots (Figure 4-4) shows some increase in SRB intensity for oleic acid treated skin at earlier times for depth greater than 15 μm. Furthermore, the addition of oleic acid leads to similar magnitude of SRB intensity at earlier time and greater depth than the control group results.

The GP image of Laurdan in skin (Figure 4-3) shows the changes of cutaneous polarity after adding oleic acid. In both the control and the oleic acid-treated group, the intercellular regions have a lower GP value than the intracellular regions. The lower GP value corresponds to a higher polarity, suggesting that the intercellular region is a better permeating pathway than the intracellular region for polar molecules.

In the control group, GP values in the intercellular regions visibly decreased with time. From the 0 μm images of control group (Figure 4-3), we observed increasingly polar solution (lower GP values) permeated from the intercellular regions to the intracellular regions.
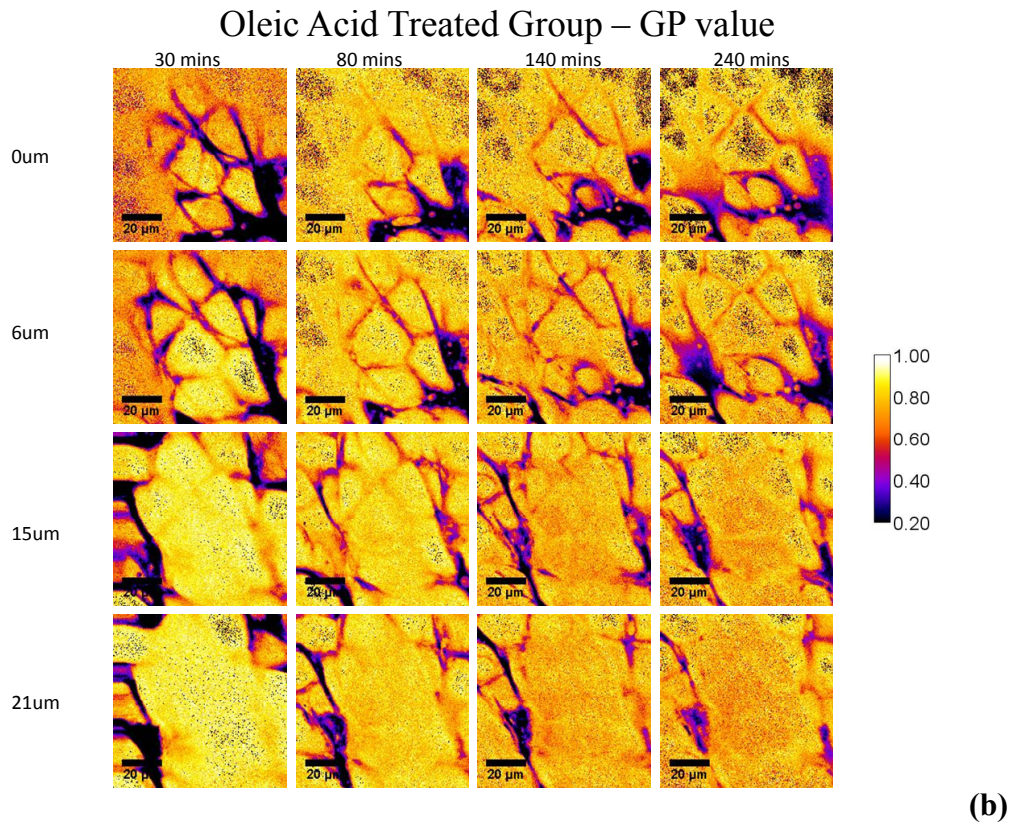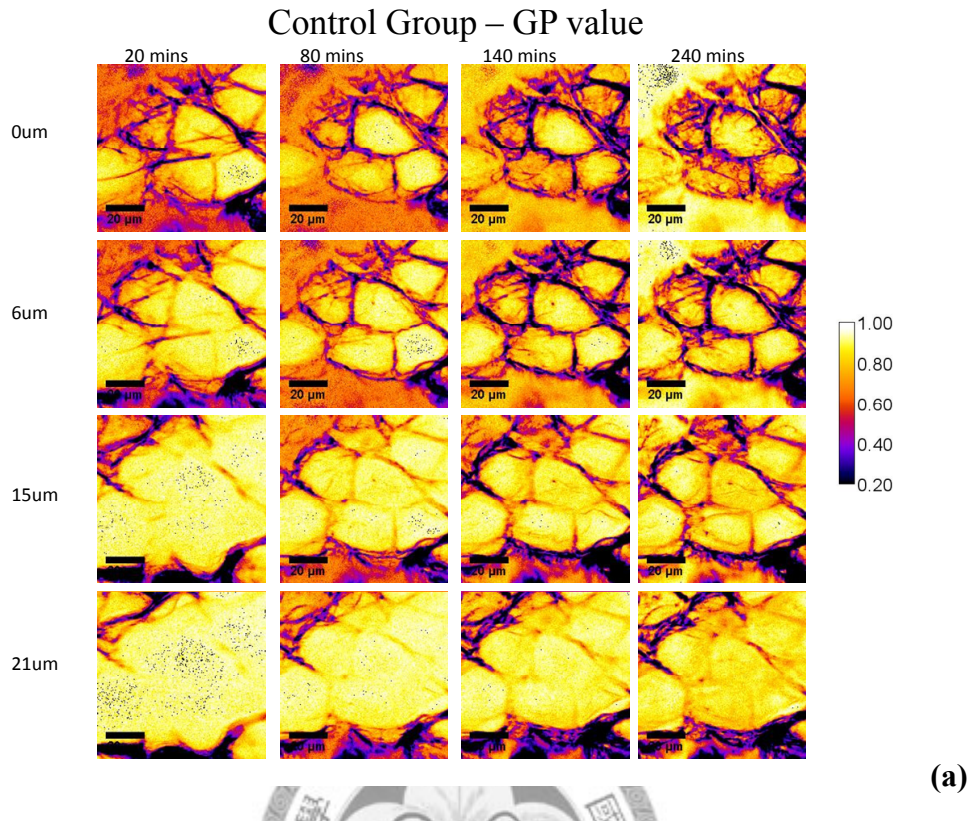
28

Figure 4-3. GP value of a selected region from (a) control and (b) oleic acid-treated groups at different depths.

To quantify the variation of SRB intensity and GP values, the general average method as described in Section 3.5 was used to determine the average SRB intensity and GP values versus skin depth. The resulting depth profiles at four different times are shown in Figure 4-4. From the general average results of the control group, it is observed that the SRB intensity increases with time at all depth. For the oleic acid-treated group, the SRB intensity reached a steady state (where the intensity no longer varies with time) less than 80 minute at depth of less than 3 μm of the skin surface, while at 140 minutes, steady SRB intensity was observed for all depths. The steady state intensity profiles of the oleic acid-treated group lie above all profiles of the non-oleic acid group. Furthermore the profiles of the non-oleic acid group have not reached steady state at 240 minutes and appear to be still rising. Comparing the SRB intensity profiles at similar times and depths, oleic acid-treated samples show greater SRB intensity than that of the control group. Therefore, the addition of oleic acid greatly increased not only the permeation rate of SRB, but the rate that the steady state permeation rate is reached.

General Average

Control

(a)

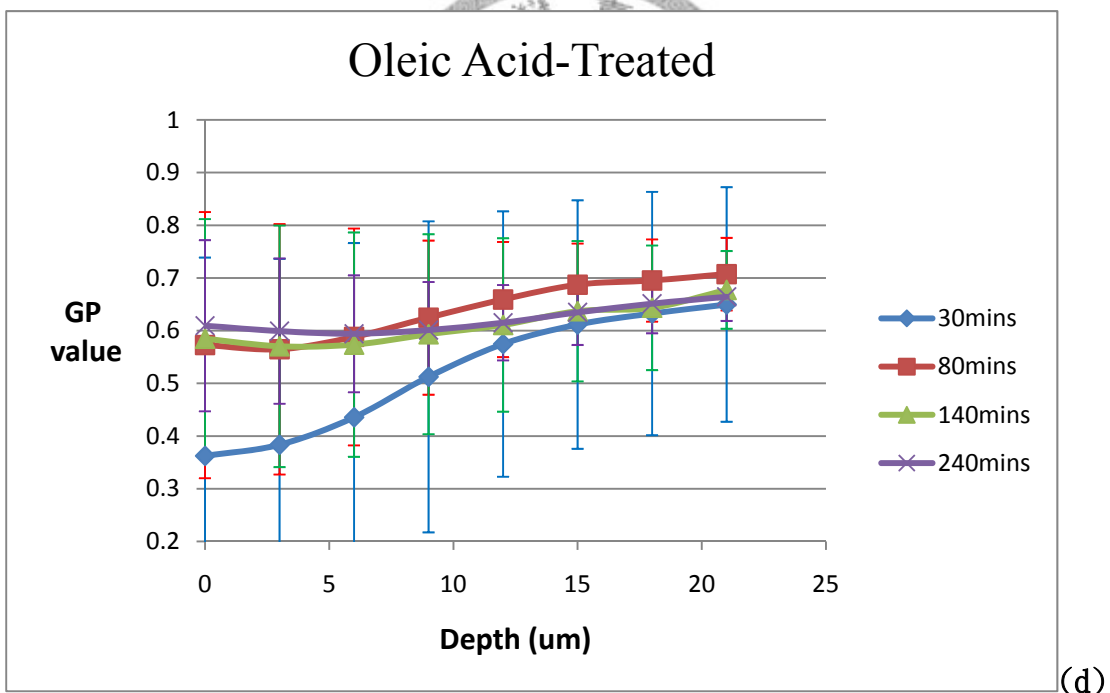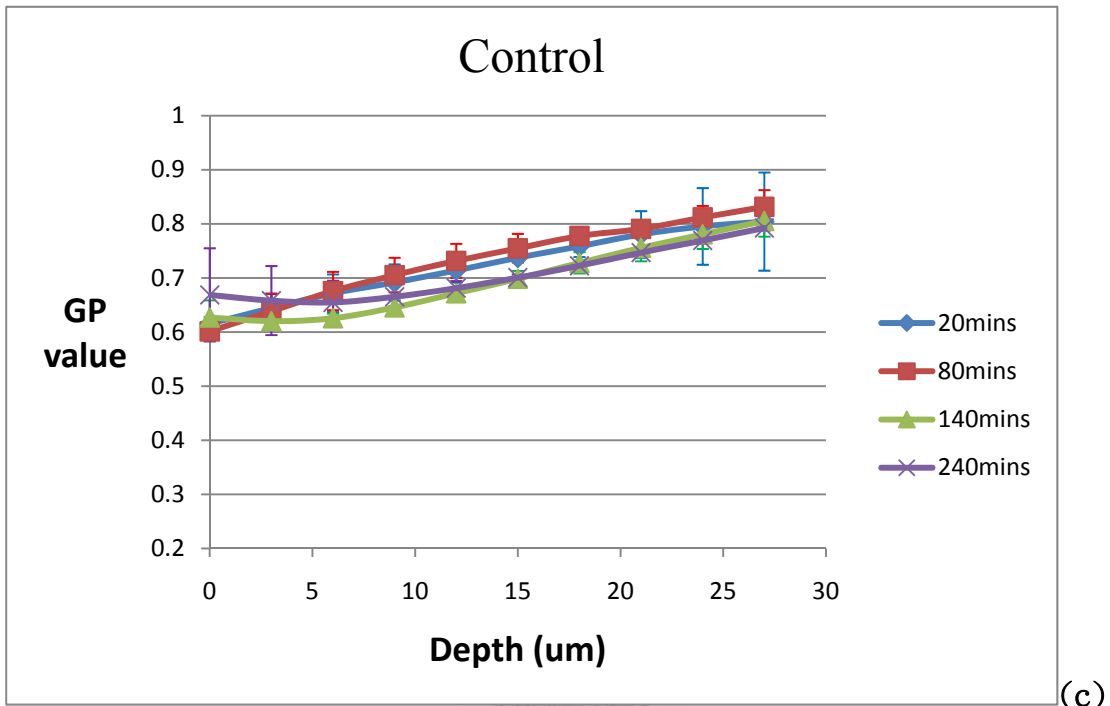## Oleic Acid-Treated

(b)

(c)

(d)
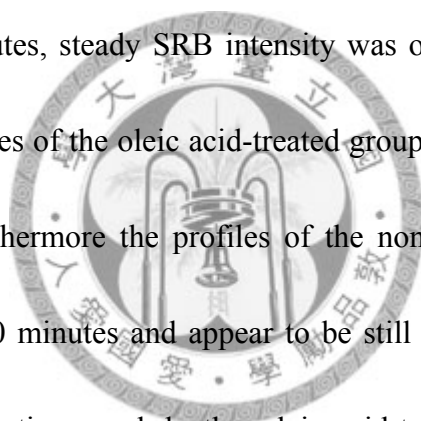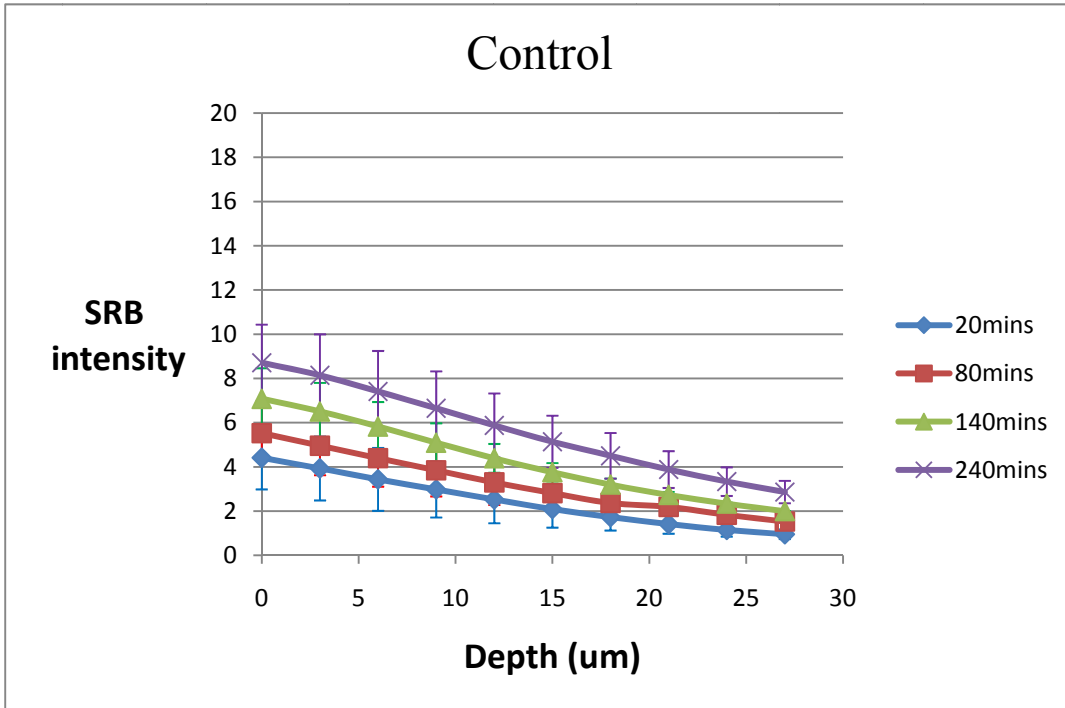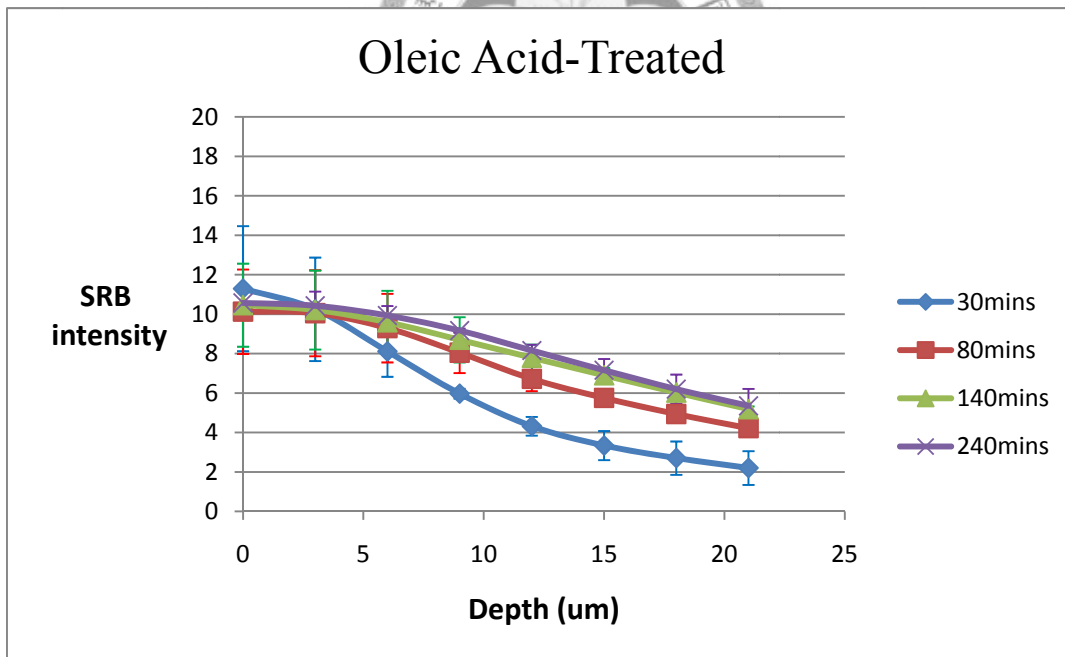
Figure 4-4. (a) and (b): General average depth profiles for different time points of SRB intensity for the control group and the oleic acid-treated group. (c) and (d): General average depth profiles for different time points of GP values for the control group and the oleic acid-treated group.

With the addition of oleic acid, the general average of GP values at depth smaller

than 10 μm increases with time, but in skin samples without the addition of oleic acid,

the general average of the GP values at similar depth remained fairly constant with time.

The different behaviors indicate changes in the polarity property within the first 10 μm

of skin surface during the first 80 minutes after adding oleic acid. A possible

explanation consistent with the result of relative magnitude of GP values for

components in solution in Section 4.1 is that the addition of oleic acid as a chemical

enhancer causes the skin to experience a chemical structural deformation[9-10] that

enhances the permeation not only for the SRB and water molecules, but also for the

other components in the solution with higher GP values than SRB and water. Therefore,

the environmental polarity changes in the skin can be attributed to molecules in solution

other than SRB and water. The GP measurements of various solutions shown in Fig. 4-1

suggest that ethanol and DMSO (but only 1% in solution) are the most possible

candidates. Additional chemical analysis for components in SC is required to verify this

inference.

As describing in Section 3.5, intercellular phospholipids region play an important

role on transdermal penetration and the interaction with chemical enhancers. To

investigate transdermal permeation in the intercellular region, areas centered around the

intercellular regions were selected from the area used by general averaging (Figure 3-4).

These selected regions were used to determine the average SRB intensity and GP values

in order to observe the contribution of this major permeating pathway to the general

permeation. Figure 4-5 shows the result of this specific averaging. From Fig. 4-5(a), we

see that the SRB intensity profile for the control group increases with time, similar to

that of the general average, but at a higher average intensity. This is consistent with the

observation (Fig. 4-2(a)) that for the control group, the permeation path of SRB occurs

mostly through the intercellular region. For the oleic-acid treated group, the specific

average intensity increases in comparison to the general average case, much like the

control group. However, the steady state profile is reached more quickly in less than 80

minutes, compared with the general averaging, indicating that oleic acid better enhances

the rate the steady state permeation rate through the intercellular region is reached.

From Fig. 4-5(c), we see that for the control group, GP values in the intercellular

regions tends to decrease with time for every depth, particularly at depth from 3 to 20

μm from the skin surface. This trend is in contrast to the results of general average,

showing that an increase in GP values occurs in non-intercellular regions in order to

obtain a fairly time constant GP values in the general average. The increase in GP value

of the non-intercellular region suggests that for the control group, there is an increase

with time in the number of non-polar molecules for intracellular regions, while the

decrease in GP value of intercellular region suggests that there is an increase in time in

the number of polar molecules for the intercellular regions.

Specific Average

Control

(a)

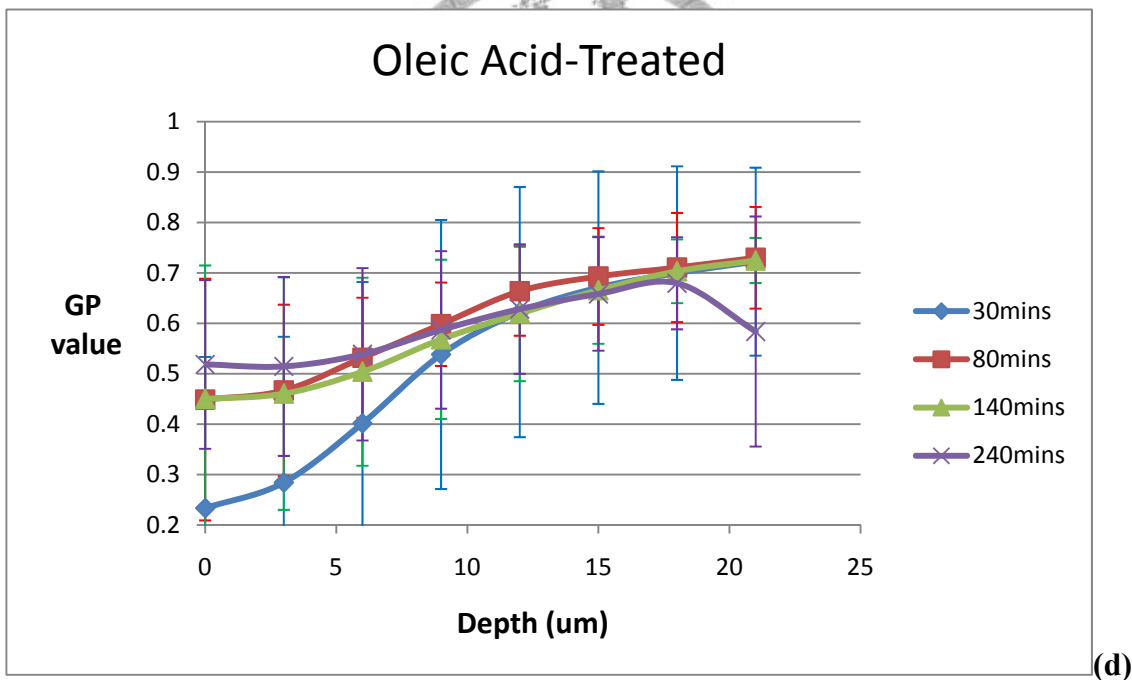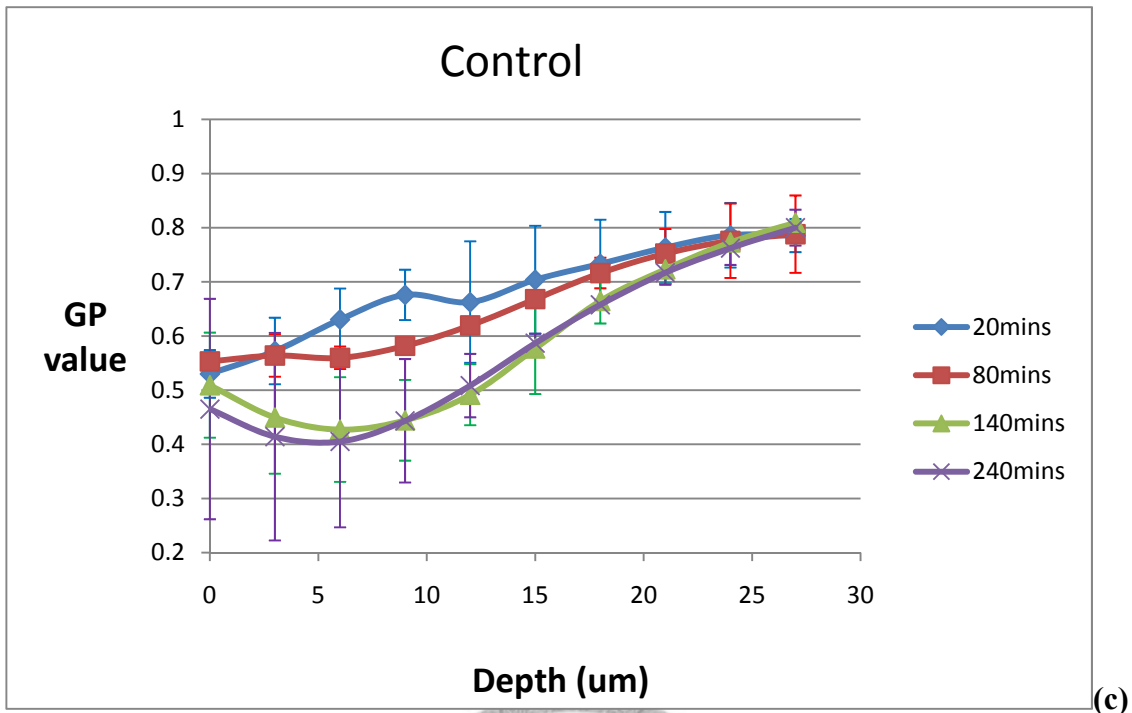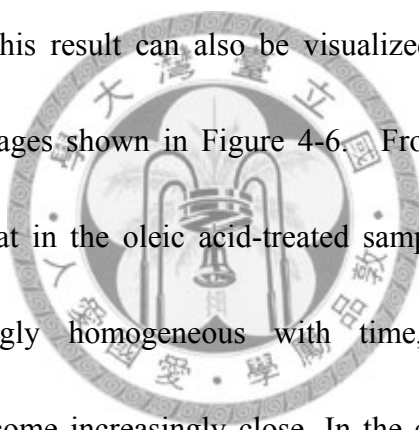## Oleic Acid-Treated

(b)

(c)

(d)
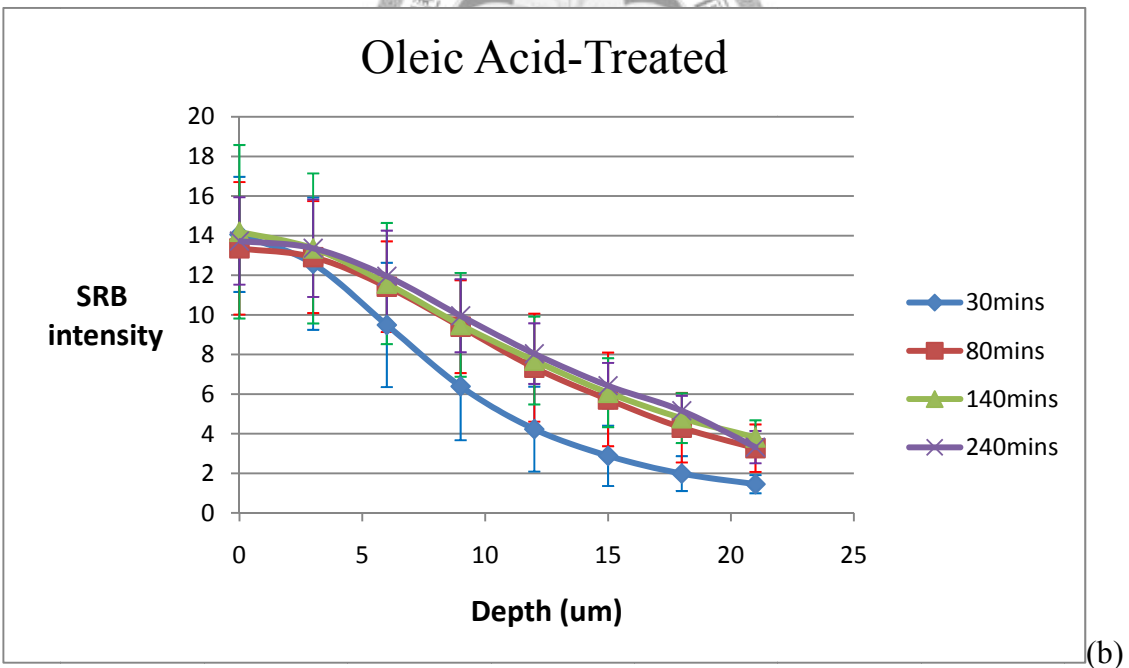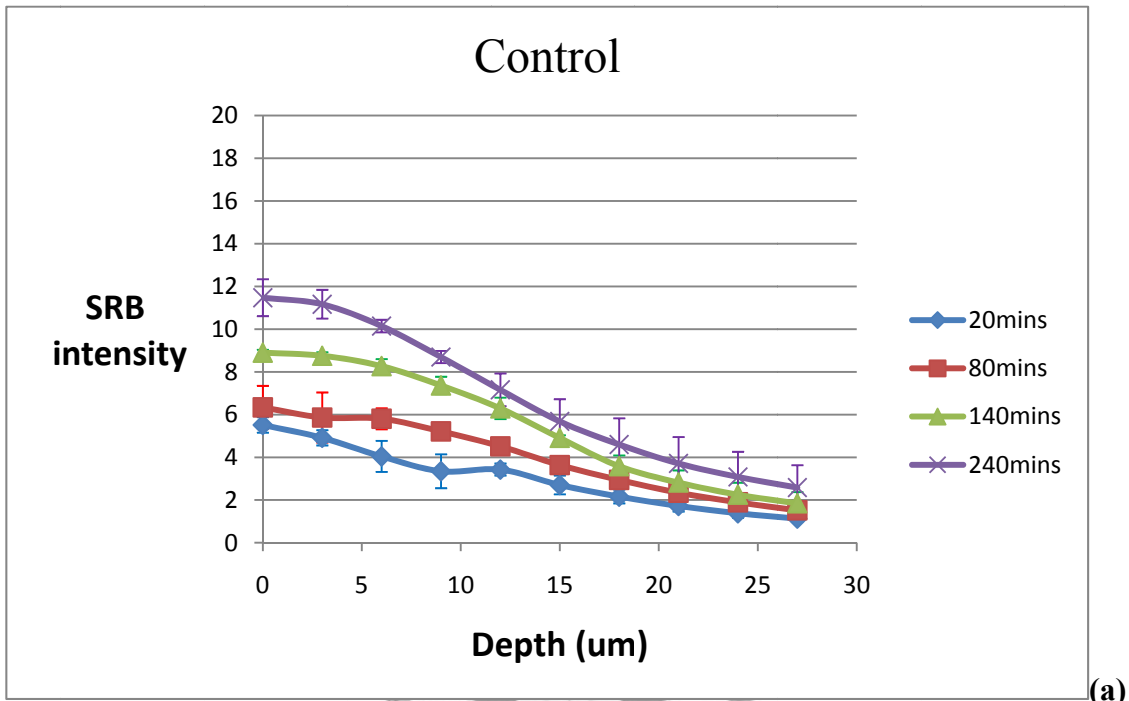
Figure 4-5. (a) and (b): Specifically averaged depth profiles at different time points of SRB intensity for the control group and the oleic acid-treated group. (c) and (d): Specifically averaged depth profiles at different time points of GP values for the control and the oleic acid-treated groups.

In the oleic acid-treated samples, both the general and specific averaged GP values show the same tendency to increase within the first 10 μm depth during the first 80 minutes. This implies that the polarity variations in the intercellular regions and the general regions are similar in oleic acid-treated samples. This is in contrast to the control group (Fig. 4-5(c) and Fig. 4-4(c)) where the specific averaged GP profiles show greater time dependence than that of the general average.   In other words, oleic acid as a chemical enhancer can promote a more uniform permeation between different regions of stratum corneum[10-11]. This result can also be visualized by the three dimensional construction of the GP images shown in Figure 4-6. From circled region shown in Figure 4-6, we observe that in the oleic acid-treated samples, the distribution of GP values become increasingly homogeneous with time, while intercellular and intracellular GP values become increasingly close. In the control group, however, the distribution of GP values remains different between the intercellular and intracellular regions.
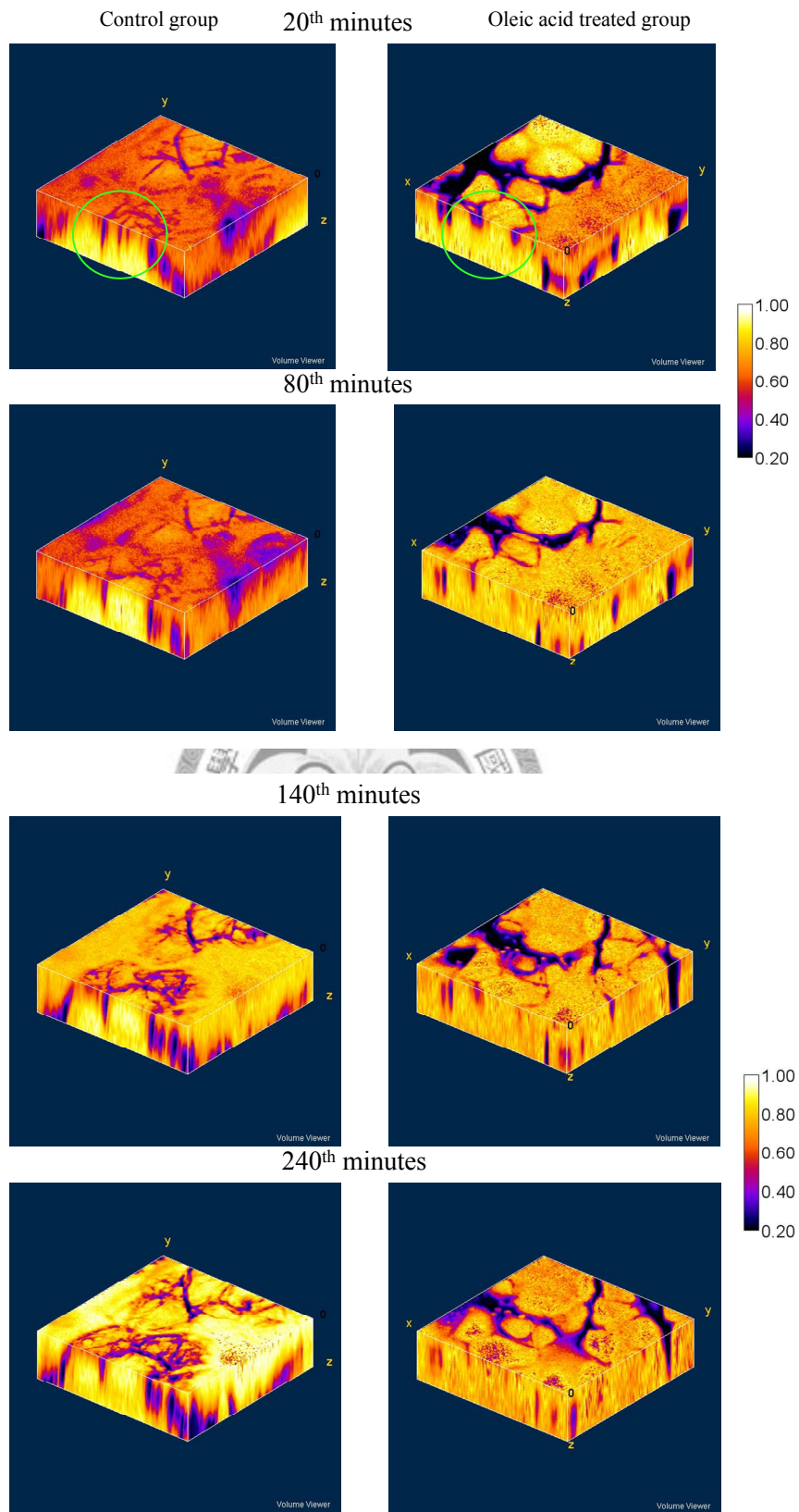
Figure 4-6. 3D GP projection for one selected regions from the control and oleic acid treated groups. Y-Z section is cross section view.

Previous works using methods of FTIR spectroscopy (Fourier transform infrared spectroscopy)[9,12], deuterium NMR[13], DSC (differential scanning calorimetry)[4,14], EM (electronic microscopy)[15] have studied the effects of oleic acid on stratum corneum from molecular interaction, thermodynamics, and structural images. In the phase-separation model, the mechanism for the improvement of the transdermal delivery due to oleic acid is described by the molecular interaction between the oleic acid and the phospholipids. As the oleic acid molecules permeates into the phospholipids-rich intercellular regions, the interface of liquid oleic acid and the ordered solid phospholipids form phase defects. In the phase defect, the hydrophobic alkyl chains of phospholipids are disturbed and liquidized to form structural defects in the intercellular lipid multilayer. Since the polar molecules pass more easily through these dispersive phase defects, the permeation barrier is decreased and the diffusion length is shortened. This is consistent with our data showing the oleic acid enhanced transdermal delivery of SRB.

In summary, addition of oleic acid leads to an increase in GP values and the rate of SRB permeation. It also results in a more homogeneous distribution in GP values for a fixed depth. Our data show that oleic acid can lower the transdermal permeation barrier or shorten the diffusion length by letting smaller polar molecules such as SRB

and higher-GP molecules such as ethanol in solution pass through skin stratum corneum

more effectively.

Chapter 5 Conclusions

In this project, we had found:

1. The relative GP values for the different solvents are $GP_{DMSO} > GP_{Ethanol} >$

   $> GP_{Ethanol:PBS=2:1} > GP_{Oleic\ Acid}$ which suggest that the order of the polarity for

   the different solvents are

   $Polarity_{DMSO} < Polarity_{Ethanol} < Polarity_{Oleic\ Acid} < Polarity_{Ethanol:PBS=2:1}$

2. Comparing the general and specific averaging of the GP value profiles suggest that

   without the addition of oleic acid, polar molecules preferentially permeate through

   the intercellular regions while non-polar molecules preferentially permeate through

   the intracellular regions.

3. Addition of oleic acid greatly increased not only the permeation rate of SRB, but the

   rate that the steady state permeation rate is reached. This was observed by

   comparing the SRB intensity profiles at similar times and depths for the oleic

   acid-treated group and that of the control group.

4. The addition of oleic acid leads to an increase in the GP value within 10 μm of skin

   surface suggest that oleic acid improved the permeation of not only polar molecules

   (SRB, water) but also other higher GP values components in the solution such as

   ethanol and DMSO.

5. The addition of oleic acid leads to a more homogeneous fixed depth distributions of SRB intensity and GP values in skin stratum corneum, revealing a significant enhancement in the intracellular permeation.

This study used the hydrophilic SRB molecules to simulate the permeation of hydrophilic drug. The resulting data demonstrated that polarity variation in skin has a large influence on the permeation of SRB molecules. A natural extension of this study is to use a molecule with similar molecular weight such as RBHE (rhodamine B hexyl ester), to observe the process of oleic acid-induced enhancement of permeation and the cutaneous polarity variation for hydrophobic molecules.
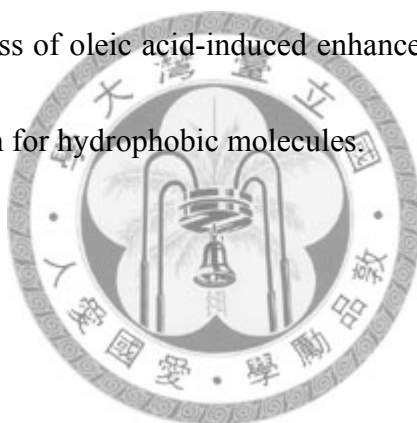
References

1   Prausnitz, M. R. & Langer, R. Transdermal drug delivery. *Nat Biotechnol* **26**, 1261-1268, doi:Doi 10.1038/Nbt.1504 (2008).

2   Kim, Y. C., Ludovice, P. J. & Prausnitz, M. R. Transdermal delivery enhanced by magainin pore-forming peptide. *J Control Release* **122**, 375-383, doi:DOI 10.1016/j.jconrel.2007.05.031 (2007).

3   Karande, P., Jain, A. & Mitragotri, S. Discovery of transdermal penetration enhancers by high-throughput screening. *Nat Biotechnol* **22**, 192-197, doi:Doi 10.1038/Nbt928 (2004).

4   Gomez-Fernandez, A. O. a. J. C. A Differential Scanning Calorimetry Study of The Interaction of Free Fatty Acid With Phospholipid Membrane. *Chemistry and Physics of Lipids* **45**, 75-91 (1987).

5   Boyd, R. W. *Nonlinear optics*. 3rd edition edn,   (Burlington, MA : Academic Press, 2008).

6   Shankar, R. *Principles of Quantum Mechanics*. 2nd ed edn,   (New York : Plenum Press, 1994).

7   G.M. El Maghraby, B. W. B. a. A. C. W. Review: Liposomes and skin: From drug delivery to model membranes. *Eur J Pharm Sci* **34**, 203-222 (2008).

8   Williams, A. C. & Barry, B. W. Penetration enhancers. *Adv Drug Deliver Rev* **56**, 603-618, doi:DOI 10.1016/j.addr.2003.10.025 (2004).

9   Ongpipattanakul, B., Burnette, R. R., Potts, R. O. & Francoeur, M. L. Evidence That Oleic-Acid Exists in a Separate Phase within Stratum-Corneum Lipids. *Pharm Res-Dord* **8**, 350-354 (1991).

10   Yu, B., Dong, C. Y., So, P. T. C., Blankschtein, D. & Langer, R. In vitro visualization and quantification of oleic acid induced changes in transdermal

transport using two-photon fluorescence microscopy. *J Invest Dermatol* **117**, 16-25 (2001).

11 Yu, B., Kim, K. H., So, P. T. C., Blankschtein, D. & Langer, R. Visualization of oleic acid-induced transdermal diffusion pathways using two-photon fluorescence microscopy. *J Invest Dermatol* **120**, 448-455 (2003).

12 Guillard, E. C., Tfayli, A., Laugel, C. & Baillet-Guffroy, A. Molecular interactions of penetration enhancers within ceramides organization: A FTIR approach. *Eur J Pharm Sci* **36**, 192-199, doi:DOI 10.1016/j.ejps.2008.10.010 (2009).

13 Seelig, A. & Seelig, J. Dynamic Structure of Fatty Acyl Chains in a Phospholipid Bilayer Measured by Deuterium Magnetic-Resonance. *Biochemistry-Us* **13**, 4839-4845 (1974).

14 M. L. Francoeur, G. M. G., and R. O. Potts. Oleic-Acid - Its Effects on Stratum-Corneum in Relation to (Trans)Dermal Drug Delivery. *Pharm Res-Dord* **7**, 621-627 (1990).

15 Shao Jun Jiang, a. X. J. Z. Examination of the Mechanism of Oleic Acid-Induced Percutaneous Penetration Enhancement: an Ultrastruxtural Study. *Biological & Pharmaceutical Bulltin* **26**, 66-68 (2003).